

TOPICAL REVIEW

## Recent progress in piezotronics and tribotronics

To cite this article: Weiguo Hu *et al* 2019 *Nanotechnology* **30** 042001

View the [article online](#) for updates and enhancements.






**IOP | ebooks™**

Bringing you innovative digital publishing with leading voices to create your essential collection of books in STEM research.

Start exploring the [collection](#) - download the first chapter of every title for free.

## Topical Review

# Recent progress in piezotronics and tribotronics

Weiguo Hu<sup>1,2,3,5,6</sup> , Chi Zhang<sup>1,2,3,5,6</sup>  and Zhong Lin Wang<sup>1,2,3,4,6</sup> 

<sup>1</sup> CAS Center for Excellence in Nanoscience, Beijing Key Laboratory of Micro-nano Energy and Sensor, Beijing Institute of Nanoenergy and Nanosystems, Chinese Academy of Sciences, Beijing 100083, People's Republic of China

<sup>2</sup> School of Nanoscience and Technology, University of Chinese Academy of Sciences, Beijing 100049, People's Republic of China

<sup>3</sup> Center on Nanoenergy Research, School of Physical Science and Technology, Guangxi University, Nanning, 530004, People's Republic of China

<sup>4</sup> School of Material Science and Engineering, Georgia Institute of Technology Atlanta, GA 30332, United States of America

E-mail: [huweiguo@binn.cas.cn](mailto:huweiguo@binn.cas.cn), [c Zhang@binn.cas.cn](mailto:c Zhang@binn.cas.cn) and [zlwang@gatech.edu](mailto:zlwang@gatech.edu)

Received 30 January 2018, revised 24 October 2018

Accepted for publication 2 November 2018

Published 30 November 2018



CrossMark

## Abstract

As the electronic technology is approaching its limits of materials and processing, a smart interaction between functional device and environment is a promising way for future electronic technology above the Moore's law. The mechanical signal triggering is the most common and natural way for the smart interactions, which has realized direct interaction between human/ambient and electronics and artificial intelligence. In 2006, the piezotronic effect, as a novel effect, was first proposed by Wang to achieve the effective, adaptive and seamless interactions between electronic devices and the external stress, which utilizes the piezoelectric polarization potential as the virtual gate to tune/control the carriers' transportation in the electronic device. Since then, this new effect has been widely observed in many low-dimensional semiconductors such as ZnO, GaN, CdS nanowires, and 2D MoS<sub>2</sub>. In extension, tribotronics was first proposed in 2014 by Wang, which is about the devices manufactured using the electrostatic potential created by triboelectrification as a 'gate' voltage to tune/control energy transformation and electrical transport in semiconductors for the smart interaction between device and environment. Tribotronics has made rapid research progress and many tribotronic functional devices have been studied with a variety of materials, such as tribotronic tactile switch, memory, hydrogen sensor and phototransistor. This review highlights advances in piezotronics and tribotronics with focus on fundamental theories, nanoscale materials, functional devices and simulations. Our emphasis is mainly about their application for third-generation semiconductor. The concepts and results presented in this review show that the piezotronics and tribotronics will facilitate the development of MEMS/NEMS, self-powered sensing, man-computer interfacing, and active wearable electronics.

Keywords: nanogenerator, piezotronics, tribotronics, nanoscale, MEMS

(Some figures may appear in colour only in the online journal)

<sup>5</sup> These authors contributed equally to this work.

<sup>6</sup> Authors to whom any correspondence should be addressed.

## 1. Introduction

The Moore's law has directed information technology in the last few decades, which drives people to fabricate CPU with the higher speed and smaller size. However, Moore's law is approaching the physical limitations of silicon. Emerging portable electronics, flexible electronic and smart human-human interfacing indicates that the multifunctionality and diversity is another development trend of future information technology [1]. Different from silicon, ZnO and GaN, the common third-generation semiconductors, simultaneously have the semiconductor and piezoelectric properties. In 2006, Wang *et al* introduced the fundamental principle of piezotronics, which uses the piezopotential generated in the third-generation semiconductors as a 'virtual gate' to tune the electrical transport in electronic devices [2–5]. This new effect can realize the effective and seamless interactions between micro/nano-electronic devices and external mechanical strain, which has great potential in designing the future electronic devices beyond the Moore's law. Recently, piezotronics received a lot of attention and were widely proved in many II–VI and III–V wurtzite semiconductor materials, such as, GaN [6, 7], InN [8], CdS [9], and CdSe [10] nanomaterials. In addition, new piezotronic materials such as Te microwire [11], Te nanobelt [12] and ZnSnO<sub>3</sub> nanowire [13], have been reported, which exhibit some new piezotronic phenomena.

In 2014, as an extension of piezotronics and new application of triboelectric nanogenerator [14, 15], an important research field of tribotronics was proposed by coupling with triboelectricity and semiconductor by Wang *et al* [16]. Tribotronics is about the devices fabricated using the electrostatic potential created by triboelectrification as a 'gate' voltage to tune/control energy transformation and electrical transport in semiconductors for human-machine interaction [16, 17]. Different from piezotronics, the selected materials for tribotronics are the general semiconductors, such as silicon [16, 18], InSb [19], pentacene [20–22] and MoS<sub>2</sub> [23, 24]. Up to now, many tribotronic functional devices have been studied including tribotronic tactile switch [23], memory [21], hydrogen sensor [25] and phototransistor [24, 26].

Here, we focus on the novel research fields of piezotronics and tribotronics. Firstly, we review the fundamental principle of the piezotronic effects in 1D materials, heterojunctions, 2D materials and their applications in the tactile imaging and logic devices. Then we summarize the tribotronics with focus on nanoscale materials, functional devices and simulations. The piezotronics and tribotronics have potential applications in self-powered sensing, human-machine interfacing, MEMS/NEMS and active flexible/stretchable electronics.

## 2. Fundamental theories of the piezotronics

### 2.1. Basic theoretical framework

Zhong Lin Wang introduced the concept of piezotronics in 2006 [2–5] and built the basic theoretical framework in later

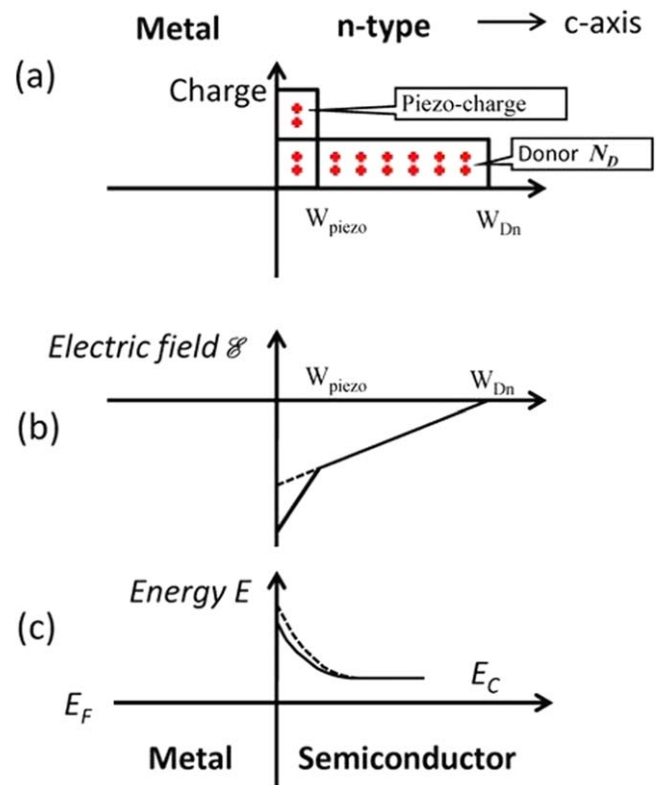


**Figure 1.** Strain modulated metal–semiconductor Schottky contact. (a) Space charge distribution. (b) Electric field. (c) Energy band diagram without (dash line)/with the piezoelectrical potential (solid line). [27] John Wiley & Sons. Copyright © 2011 WILEY-VCH Verlag GmbH & Co. KGaA, Weinheim

works [27]. The piezotronics is simultaneously utilizing the piezoelectric property and the semiconductor property. The basic theoretical framework includes three main equations, (i) the constitutive equations which reveal the distribution of the piezoelectric field and the strain field; (ii) Poisson equation which reveals the distribution of electric field; (iii) the classic drift-diffusion equations which reveal the carrier transportation under the electric field. These equations can be solved with various mathematical methods such as the numerical calculation based on the finite element method (FEM) and the analytic method. The first one can give a clear spatial distribution of the strain, piezoelectric polarization, and charges and the latter can be easily used to fit experimental results. The typical example of piezotronic devices is based on the strain-modulated metal–semiconductor Schottky contact. Figure 1 shows the distribution of the space charge, the electrical field and the energy band in strain modulated metal–semiconductor Schottky contact. When the strain is applied on the metal–semiconductor Schottky contact, the piezoelectric semiconductor such as ZnO induces piezoelectric polarization charges at the interface between metal and semiconductor. This high-density and fixed charges change the Schottky barrier height (SBH) and the depletion width, which finally control the carriers' transportation. For a metal/wurtzite nanowire piezotronic transistor, the analytic resolution is given as

below [27]:

$$J = J_{D0} \exp\left(\frac{qe_{33}s_{33}W_{piezo}}{2\varepsilon_s kT}\right) \left[\exp\left(\frac{qV}{kT}\right) - 1\right], \quad (1)$$

where the  $J_{D0}$  is the saturation density in the absence of piezoelectric charges,  $s_{33}$  is the axial strain,  $e_{33}$  is the piezoelectric coefficient,  $W_{piezo}$  is the width of the piezoelectric charge. The equation shows that the current across the Schottky contact is an exponential function of the strain. Thus, the strain can act as the virtual gate to effectively control the current in the metal–semiconductor piezotronic transistor. This analytic resolution provides a simple and effective method to analysis the  $I$ – $V$  measurements. This theoretical framework is also used to deduce another piezotronic devices such as  $p/n$  junction.

## 2.2. First principle calculation

The classic constituter equations only treat the piezoelectric materials as the bulk materials. However, the piezoelectric charge is strongly localized at the interface and depends on the polarization direction. The width of the piezoelectric charge is an important physical parameter. Based on the first principles of quantum mechanics, Wang *et al* further take the density function theory and Poisson equation to calculate the piezotronic effect in a metal–semiconductor–metal piezotronic transistor, as shown in figure 2 [28]. The electrostatic potential is calculated with the Vienna *ab initio* simulation package with the frozen-core projector-augmented-wave pseudopotentials. And the charge density from the electrostatic potential is calculated from the Poisson equation. The classical piezoelectric theory assumes piezoelectric charges fixed at the very interface expected to be one or two atomic layers. And this research firstly reveals the atomic scale fluctuation of piezoelectric charges. The widths of piezoelectric charges are 4.1 and 3.7 Å at Ag–ZnO (000-1) and Ag–ZnO (0001) junctions, respectively, which agree with the assumption in the piezoelectric theory, and strongly depends on the applied strain.

Finally, the SBH under the strain is calculated by using the bulk-plus-lineup method [28]:

$$\Phi_B = E_g - [E_f - (\bar{V} + \Delta)], \quad (2)$$

where  $E_g$  is the bandgap of bulk ZnO,  $E_f$  is the Fermi level,  $\bar{V}$  the macroscopic average potential in the interface region, and  $\Delta$  is the energy difference between the valence band edge and the average potential in bulk ZnO. Calculated results clearly reveal the strain modulation on the SBH, for example 0.5 meV shift under 1% tensile/compressive strain, which match well with the previous experimental results. This work proves the piezotronic effect from the magnitude of atomic scale for the first time and deepens our understanding on the atomic scale distribution of piezoelectric charge.

Based on the *ab initio* density theory, Migliorato *et al* calculated the nonlinear piezoelectric coefficients in III–V [29] and II–VI semiconductors [30]. The polarization term is

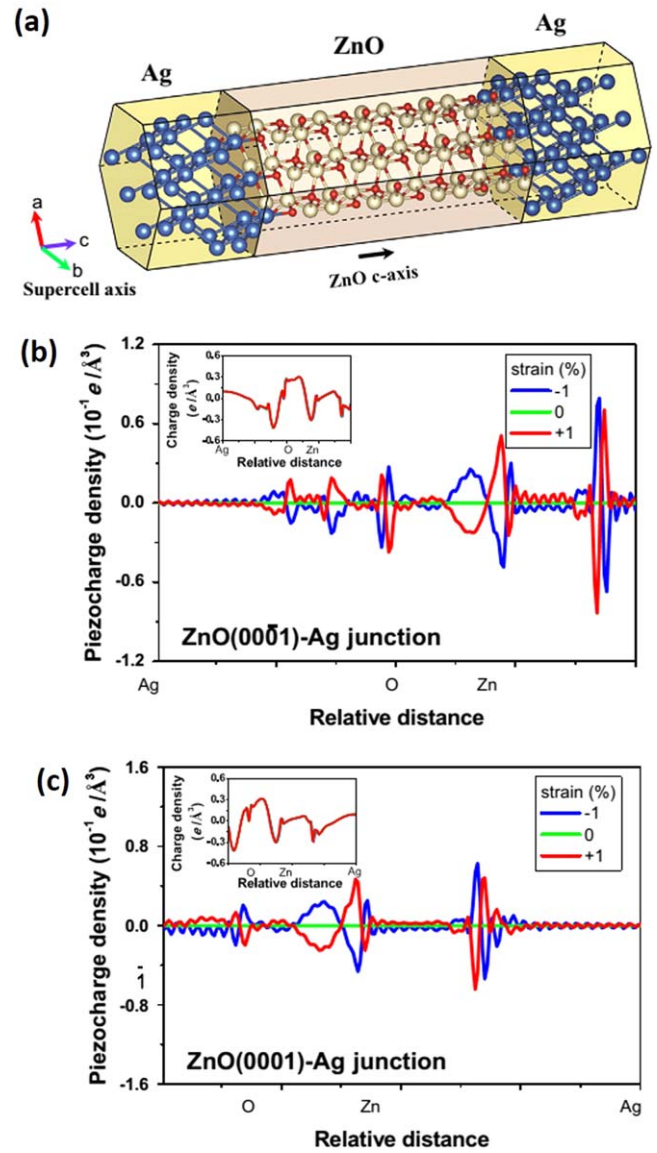


**Figure 2.** First principle calculation. (a) Atomic structure model of an Ag–ZnO–Ag piezotronic transistor. (b) Piezoelectric charge distribution at ZnO (000-1)-Ag interface with  $\pm 1\%$  strain. (c) Piezoelectric charge distribution at ZnO (0001)-Ag interface with  $\pm 1\%$  strain. Reprinted from [28], Copyright 2015, with permission from Elsevier.

given as the sum of dipole contribution and bond polarity

$$P_{\hat{x}_i} = \frac{Z_H^* \delta r + 2a_p(1 - a_p^2) \cdot \sum_{q=1}^4 (\leftrightarrow r_q \cdot \hat{x}_i) \delta R_q}{2\Omega}, \quad (3)$$

where,  $\hat{x}_i$  is the Cartesian direction,  $Z_H^*$  is the atomic charge,  $\delta r$  is the displacement vector of cations in respect of anions from the ideal position,  $a_p$  is the bond polarity,  $r_q$  and  $\delta R_q$  are the distance and displacement vectors of the nearest neighbor  $q$  from the atom at the center of the tetrahedron, respectively,  $\Omega$  is the atomic volume. Their calculation reveals that the nonlinear piezoelectric coefficients significantly change the total strain-induced polarization in III–N alloys and ZnO. This model was also used to calculate the output voltage in III–V core–shell nanowires under the strain, which predicts that the

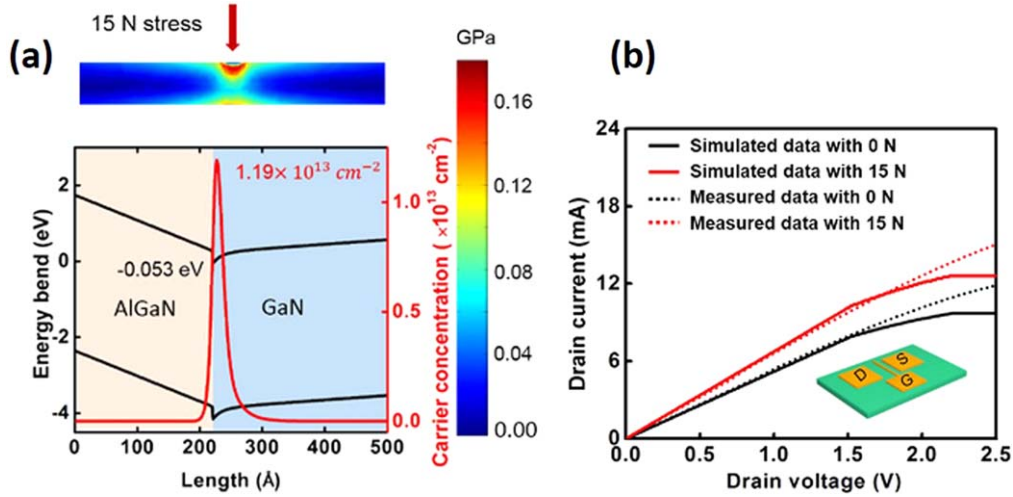


**Figure 3.** The calculated  $I$ - $V$  curves and electrical measurements. (a) Energy band diagram of AlGaN/GaN heterojunction. (b) Simulated  $I_{DS}$ - $V_{DS}$  characteristics of HEMT with 15 N stress (red solid line) and without stress (dark solid line) at  $V_{GS} = -2$  V. The scattered points are the experimental results. Reproduced from [34]. © IOP Publishing Ltd. All rights reserved.

largest core voltages is 3 orders of magnitude larger than the that in homogeneous nanowires [31]. These researches on nonlinear piezoelectricity are the significant progress, which give a close match to the piezoelectric fields of quantum well, superlattice and nanowires.

### 2.3. Poisson-Schrödinger calculation for piezotronic high electron mobility transistor (HEMTs)

With the development of nanotechnologies, the size of piezotronic devices is shrunk and the structure of them become complex. The AlGaN/AlN/GaN heterostructures microwire has been synthesized to isolate the conducting channel from the dopant ionized center [32]. And then, the strain modulated HEMTs have been fabricated [33, 34]. Due to the strong spatial localization of carriers, the quantum effect becomes a significant issue. The Schrödinger equation in the effective mass approximation is induced into the classic theoretical framework of piezotronics to explain the physical process in the quantum-piezotronic devices [34]

$$-\frac{\hbar^2}{2} \frac{d}{dx} \left[ \frac{1}{m^*} \frac{d\psi(x)}{dx} \right] + [V(x) - E]\psi(x) = 0, \quad (4)$$

where  $\hbar$  is the reduced Planck constant,  $m^*$  is the electron effective mass,  $V(x)$  is the potential energy,  $E$  is to the energy of the sub-band and  $\psi(x)$  is the wave function. The spontaneous and piezoelectric polarization induces a delta-shape potential well at the interface between AlGaN/GaN heterojunctions, where carriers are strongly localized to form quantized levels. When the external strain is applied on the device, the depth of the potential well is changed and thus affects the carrier density at the conducting channel. The carrier density is induced into the classic devices functions to

calculate the source-drain current [34]

$$I_{DS} = \begin{cases} \beta V_T [V_{DS} - (R_S + R_D) I_{DS}] \\ \beta \left( V_{GS} - V_T - \frac{1}{2} V_{DS} \right) V_{DS} \\ \beta V_L [\sqrt{V_L^2 + (V_T - R_S I_{DS})^2} - V_L] \end{cases}, \quad (5)$$

where the upper equation describes current at linear region, the middle equation describes current at the nonlinear region and the below equation describes the saturation current whose bias reaches the critical electric field for the electron velocity saturation. The figure 3 exhibits the calculated  $I$ - $V$  curves and electrical measurements. It shows that the piezoelectric potential induced by the external strain acts as a 'virtual gate' bias to control the depletion region. A good agreement between the calculated results and the experimental results is demonstrated, especially in linear region and nonlinear region. And very minor differences exist in saturation region. The saturation current is strongly affected by the kink effect, which is commonly related to surface states or defects inducing by various processes.

Beside the HEMT, some new quantum-piezotronic phenomena have been observed, for example the piezotronic modulated spin-orbit coupling. The fundamental theories of piezotronic should be further developed and deepened to explain novel phenomena and simulate new devices.

## 3. Piezotronics in low-dimensional semiconductors

### 3.1. Piezotronic effect in GaN 1D materials

The piezotronic effect is firstly introduced in the ZnO and then is observed in various II-VI and III-V wurtzite semiconductors, such as, GaN, InN, CdS, and CdSe nanowires. III-nitrides are another ideal piezotronic materials which have wide applications such as solid-state lighting, displaying, data recording, UV

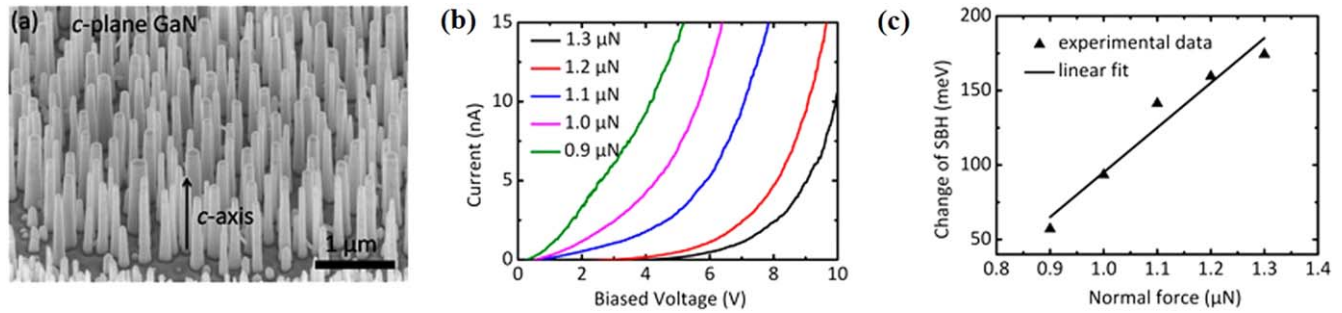


**Figure 4.** Piezotronic effect in GaN 1D materials. (a) *c*-plane GaN fabricated by the top-down process. (b) Conductive atomic force microscopy under strains. (c) The dependence of Schottky barrier height change on the normal force. Reprinted with permission from [35]. Copyright © 2015, American Chemical Society.

detector, electric/electrical devices, photovoltaics and so on. In figure 4, the polarity control on GaN NWs is fabricated with the top-down etching process [35]. By applying 0–1.3 μN normal compressive force, the source–drain current of *c*-plane GaN NWs exhibit a remarkable and monotonous decrease and the shift of SBH was deduced to be 176 meV. However, this modulation cannot be observed in the nonpolar GaN NWs (*m*-plane GaN). The comparison proves that the piezotronic effect rather than the piezoresistive effect dominated the carrier transportation changes under the strain. Liu *et al* systematically investigated the effect of carrier concentration in GaN NWs on the screen effect aroused by the carriers in piezotronic devices. With increasing carrier concentration from  $10^{17} \text{ cm}^{-3}$  to  $10^{19} \text{ cm}^{-3}$ , the force sensitivity values decrease from  $26.20 \pm 1.82$  to  $14.70 \pm 2.21 \text{ meV nN}^{-1}$  [36]. It is attributed to that at the higher free electron concentration, the more piezoelectric potential is screened, leading to smaller changes in the SBH. Besides, piezotronics in various axial orientational semiconductors, i.e. *c*-axial, *m*-axial, and *a*-axial 1D nanostructures has further been investigated [37, 38]. These researches deepen our understanding on the piezotronic effect and reveal great potential of III-nitrides in the human–machine interfacing and MEMS.

### 3.2. Piezotronic modulated heterojunction electron gas in AlGaN/AlN/GaN heterostructures

The low mobility is a significant hindrance for 1D electronic devices. A main degradation of carriers' mobility is scattered from the ionized dopant. Wang *et al* fabricated AlGaN/AlN/GaN heterojunction microwire with the metalorganic chemical vapor deposition, as shown in figure 5 [32]. In this structure, the major carriers are localized at the potential well at the interface which are spatially separated from defects or dopants in the barrier. The electrical measurements show that the mobility of AlGaN/AlN/GaN MW is remarkably increased compared to that of the GaN MW. The source–drain current can be effectively tuned with the external strain which is attributed to that the piezoelectric charges induced by the external strain lift/deepen the potential well at the interfaces to decrease/increase carriers density. The measured *I*–*V* curves matches well with the theoretical calculation. Besides, with decreasing the temperature from 300 to 77 K, the relative changes of conductance are greatly increased to

890% and 940% for compressive strains and tensile strains, respectively, which indicates a greatly enhanced piezotronic effect at the low temperature. This work provides a new freedom degree to fabricate the novel HEMT responding to the external mechanical stimuli. Wang *et al* have fabricated the strain modulated AlGaN/GaN unpassivated HEMT and metal-oxide-semiconductor (MOS) HEMT. Both unpassivated HEMT and MOS HEMT exhibits a modulation of source–drain current under the gate bias from 0 to  $-4 \text{ V}$ , just like an additional ‘virtual gate’. In addition, MOS HEMT partly compensated surface states to effectively decrease the gate leakage current [33, 34]. This new device has potential applications in the safety power device and MEMS.

### 3.3. Piezotronics in single-atomic-layer MoS<sub>2</sub>

Piezotronics goes towards new materials, such as Te and ZnSnO<sub>3</sub>. Among them, 2D piezotronic materials are an important direction with great advantages of high crystallinity and flexibility. Wang *et al* reported the first experimental evidence of the piezotronic effect in the 2D MoS<sub>2</sub> [39]. Figure 6 shows the few-layer MoS<sub>2</sub> flakes mechanically exfoliated onto a polymer stack and the layer thickness is measured by an atomic force microscopy and Raman spectroscopy. And then MoS<sub>2</sub> flakes were transfer to a polyethylene terephthalate (PET) flexible substrate and Cr/Pd/Au (1 nm/20 nm/50 nm) pair contacts were deposited along the ‘zigzag’ direction of MoS<sub>2</sub>. For a single-layer MoS<sub>2</sub>, remarkable voltage and current outputs were observed with various mechanical stimuli. The current and voltage responses to the mechanical stimuli were also observed in odd layers MoS<sub>2</sub> and disappeared in even layers MoS<sub>2</sub>. It is aroused by that the odd layer MoS<sub>2</sub> breaks the inversion symmetry to induce the piezoelectrical polarization. However, the even layer or bulk MoS<sub>2</sub> is centrosymmetric. In addition, the current responds in bilayer and bulk MoS<sub>2</sub> flakes are dominated by the pure piezoresistive effect. The gauge factors are 230 and 200 for the bilayer and bulk MoS<sub>2</sub> flakes, respectively, which are comparable to the traditional silicon strain sensor, 40–200 times than metal strain sensors and 100 times than graphene sensor. It indicates a great potential in highly sensitive strain sensors. Finally, the array integration of single-layer MoS<sub>2</sub> flakes was proved: the output voltage proportionally increases with the serial connections; and the

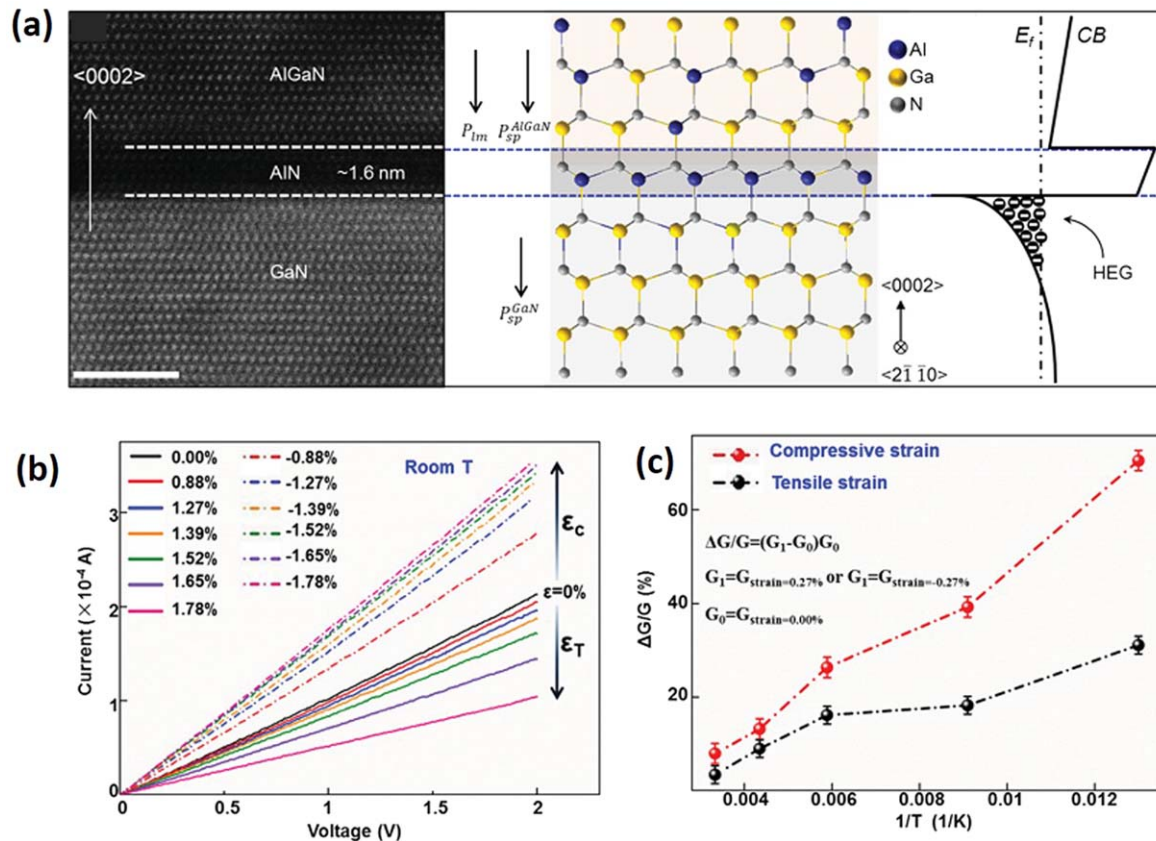


**Figure 5.** Piezotronic modulated heterojunction electron gas in AlGaIn/AIn/GaN heterostructures. (a) AlGaIn/AIn/GaN heterojunction atomic structure and energy band diagram. (b) Source–drain current under the strain. (c) Dependence of relative changes of conductance under compressive (red) and tensile (black) strains on the temperature. [32] John Wiley & Sons. © 2016 WILEY-VCH Verlag GmbH & Co. KGaA, Weinheim

output current proportionally increases with the parallel connection. It means a possibility to fabricate the large-scale MoS<sub>2</sub> piezotronic arrays. This research is an important start-up of 2D piezotronic devices, which exhibits remarkable advantages in wearable technology, strain sensors and mechanical energy collecting devices

#### 4. Smart piezotronic devices

Since piezotronics were introduced by Wang at 2006, a series of novel piezotronic devices have been reported, such as strain-gated transistor (SGT) [40, 41], logic device [6, 42], environment/biomedical sensor [43, 44], HEMT [33, 34], tactile imaging [40, 45, 46] and so on. These devices have great potential in human–machine interfacing, robotics, smart skin, environment monitoring, mechanical energy harvesting, health and medical devices and so on. Some typical devices are introduced as below.

##### 4.1. Piezotronic logic device

Logic devices are the important component of the micro-electronic technology. Recently, GaN NB based piezotronic logic devices have been fabricated to achieve various logical operations on the inputting mechanical stimuli [6]. In figure 7, GaN NBs were mechanically derived from thin solid GaN

films and then transferred on the polystyrene (PS) flexible substrate. The basic unit, SGT, takes the metal–semiconductor–metal structure and Ag/ZnO contact acts as the strain modulated Schottky junction. According to the piezotronic effect, when strains are applied along the c-axis, the negative/positive potentials are induced to effectively lift/lower the SBH to decrease/increase the source–drain current, which corresponds to ‘on’/‘off’ state, respectively. The on-off ratio is 95.7. Piezotronic logic devices exhibit very minor noise margins. For example, a GaN NB piezotronic inverters have 1.94 V and 0.017 V output levels at 2 V and 0 V theoretical values, respectively. The threshold strain gate is  $-0.43\%$ . And NOT, AND, OR, NAND, NOR, and XOR logic operations are achieved with the basic SGT unit. Moreover, a basic piezotronic computing, the one-bit binary number addition, are also demonstrated.

##### 4.2. Active and adaptive tactile imaging

Tactile sensing is the particular means to acquire information from outside environment. However, it remains difficult to be mimicked with the common electronic devices. Traditional silicon electronics hardly directly interface mechanical stimuli. And integrating pressure sensors into circuit faces great challenges in the device density and spatial resolution. By integration large-scale piezotronic strain-gated transistors into an active taxel-addressable SGT

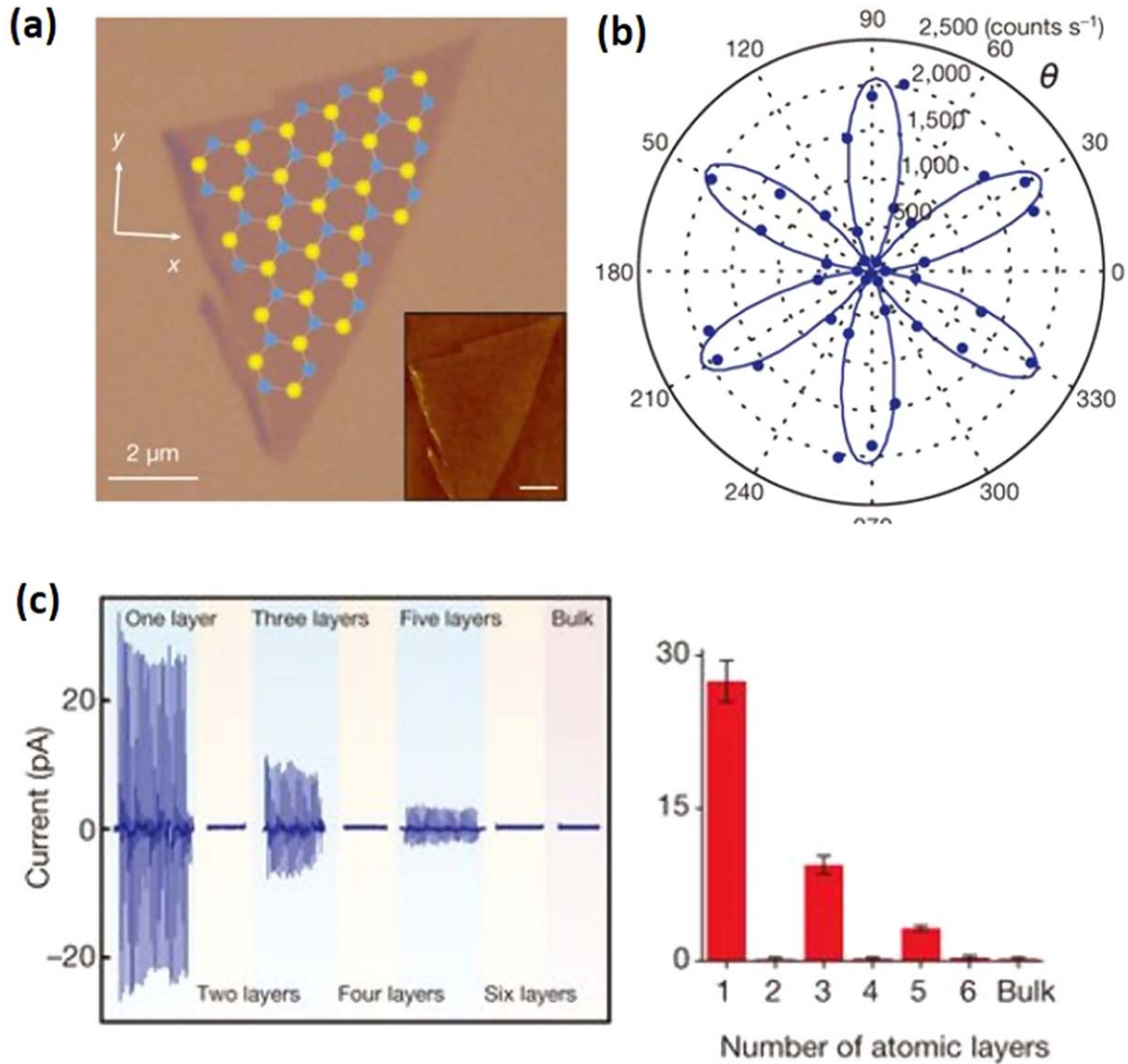


**Figure 6.** Piezotronics in single-atomic-layer MoS<sub>2</sub>. (a) Optical image of the single-atomic layer MoS<sub>2</sub> flake. (b) Polar plot the second-harmonic (SH) signal intensity as a function of the crystal's azimuthal angle. (c) The dependence of the output current on the number of atomic layers. [39] 2014 © Springer Nature. With permission of Springer.

array, Wang *et al* achieved the spatial tactile sensing. The  $92 \times 92$  ZnO SGT array is fabricated by combing patterned in-place growth and state-of-the-art microfabrication techniques, as shown in figure 8 [40]. Individual SGT responses to the external mechanical stimuli based on the classic metal–semiconductor piezotronic effect, where Au–ZnO contact is chosen as the strain modulated Schottky junction. The oxygen plasma treatment is taken to improve the quality of Schottky junction. With it, the SBH increases to  $0.575 \pm 0.013$  eV and the ideality factor reaches  $2.17 \pm 0.33$ . The sensitivity of an SGT is around  $2.1 \mu\text{S kPa}^{-1}$ . The spatial resolution is as high as 234 dpi. This device also exhibits excellent chemical and mechanical stabilities. This work provides a new method to design the tactile imaging device with the high spatial resolution. Recently, Wang and Qing further improve the spatial resolution to 12 700 dpi with hexagonal ZnO nanoplatelets array [45]. And a new function, simultaneously tactile imaging and recording, are realized

by integrating WO<sub>3</sub>-film electrochromic device array and a ZnO-nanowire-matrix pressure sensor [46]. These active and adaptive tactile imaging devices have great potential in human–machine interfacing, robotics, fingerprint identification, electronic skin and biomedical therapy.

## 5. Fundamental device of tribotronics

The conventional field-effect transistor (FET), which is using an external voltage to tune/control the charge carrier transport in a semiconductor material, has been deeply studied and widely applied in integrated circuits and Internet of Things [47, 48]. In 2014, an external force triggered/controlled contact electrification FET (CE) has been fabricated coupling TENG and MOSFET (figure 9(a)). Different from the traditional FET, the carrier transport in CE-FET is tuned/controlled by the contact-induced electrostatic potential, which is



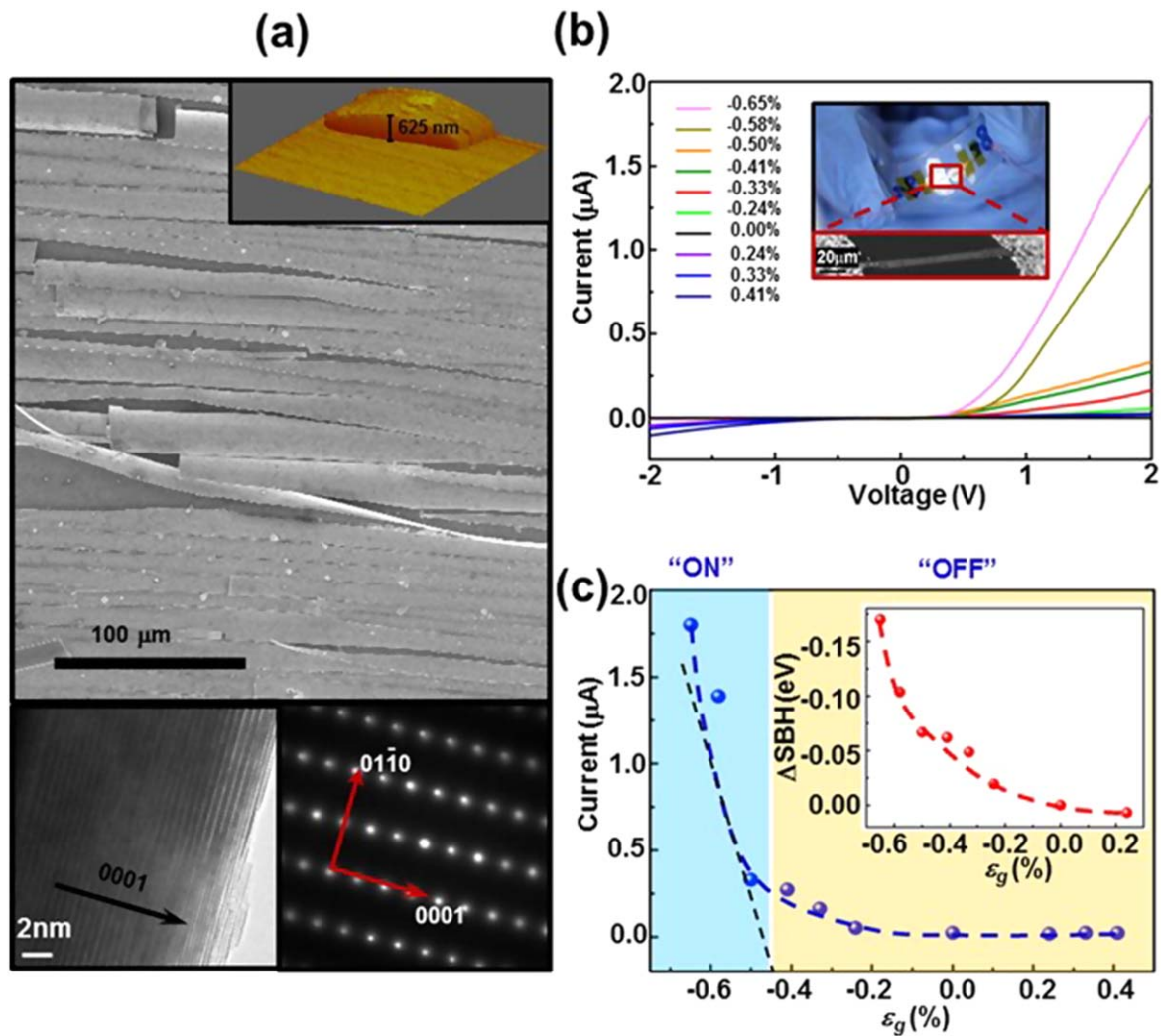


**Figure 7.** Piezotronic logic device (a) scanning electron microscopy (SEM) images and high-resolution transmission electron microscopy (HRTEM) image of GaN NB. (b) IV characteristic under strains. (c) The current as a function of strain at the fixed bias of 2 V and the dash line indicates the threshold gate strain  $-0.43\%$ . Reprinted with permission from [6]. © 2013, American Chemical Society.

created by a vertical CE between a ‘foreign’ object and the gate material (figure 9(b)) [16]. Based on the fundamental CE-FET, various interactive functional devices are achieved and an original field of tribotronics is opened up.

Tribotronics is about the devices fabricated using the electrostatic potential created by triboelectrification as a ‘gate’ voltage to tune/control energy transformation and electrical transport in semiconductors for human–machine interaction [16, 17]. As an original and novel invention, tribotronics is an important application of TENG and could open up the road to more important potential applications in the fields of active flexible electronics, human–machine interactive system and wearable electronics.

## 6. Tribotronics in 2D materials

### 6.1. Graphene tribotronics for electronic skin

Graphene, a quasi-two-dimensional (2D) material, is a monolayer of  $sp^2$ -bonded carbon atoms. Recently, owing to

the excellent electronic transport characteristics and physical properties, graphene has been attracted great interest. Most remarkably, graphene has ambipolar transport characteristics and it can be charged with either negative or positive charges after rubbing, which means that graphene is an ideal material for tribotronic devices. A graphene tribotronic touch sensor composed of a graphene FET and a coplanar single-electrode-mode triboelectric nanogenerator (S-TENG) is developed [49] (figure 10(a)). The S-TENG is consist of an indium tin oxide (ITO) bottom electrode with an poly(dimethylsiloxane) (PDMS) friction layer, and coupled with the grapheme channel in a coplanar fashion by a 1-ethyl-3-methylimidazolium bis(trifluoromethylsufonyl)imide ([EMI][TFSI])-based ion-gel gate dielectric. When any external object contact with the PDMS friction layer, carrier transport of the graphene FET can be tuned by the triboelectric potential, just like the traditional ‘gate’ voltage. As a touch sensor, the device shows good sensing performances that the touch sensitivity can reach to  $2\% \text{ kPa}^{-1}$ , the detection limit is less than 1 kPa and the response time is about 30 ms (figures 10(b), (c)). In

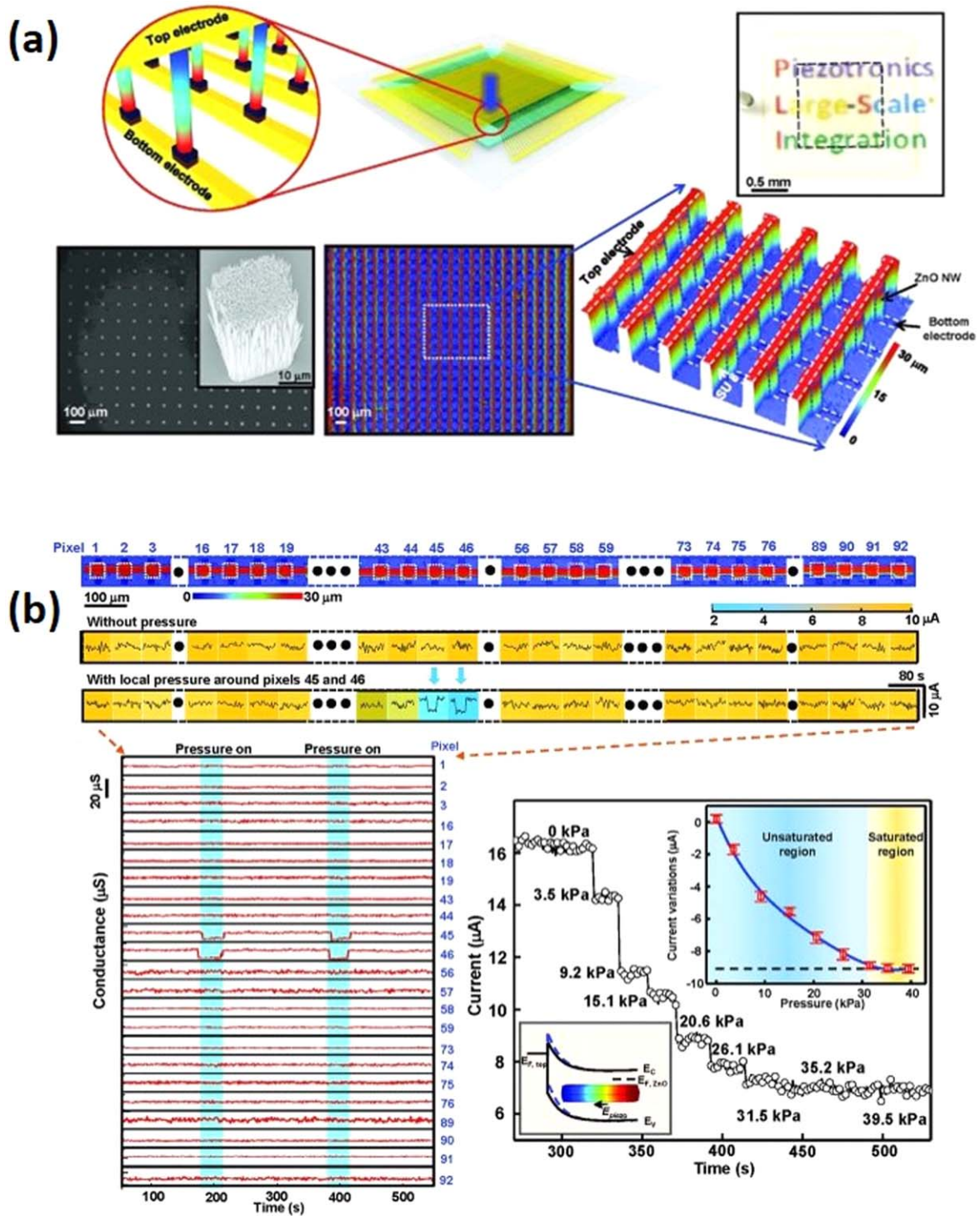


**Figure 8.** Active and adaptive tactile imaging. (a) Schematic illustration, optical image and scanning electron microscopic images of 3D strain gate transistor array. (b) Single-channel line scanning electrical measurement for SGT array device. From [40]. Reprinted with permission from AAAS.

addition, different from the capacitive touch sensors, the touch stimuli with gloved fingers can also be effectively detected by the graphene tribotronic sensors. Furthermore, a  $3 \times 3$  graphene tribotronic sensors array is demonstrated and attached on the wrist to multiple finger touch stimuli (figure 10(d)). The trajectory of the moving ball can be

accurately detected by the graphene tribotronic array. Besides, the graphene tribotronic devices have the advantages of transparent, flexible, and simple construction. Therefore, based on these advantages, the graphene tribotronic devices has application potentials in ultrasensitive e-skins and artificial intelligence.

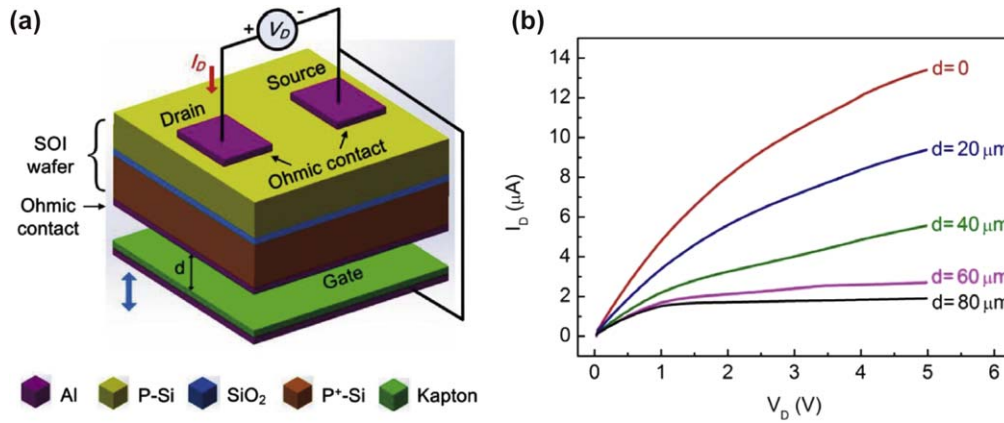


**Figure 9.** Fundamental device of tribotronics. (a) Schematic diagram of the CE-FET. (b)  $I_D$ - $V_D$  output characteristic curves of the CE-FET at different vertical distances. Reprinted with permission from [16], Copyright 2014 American Chemical Society.

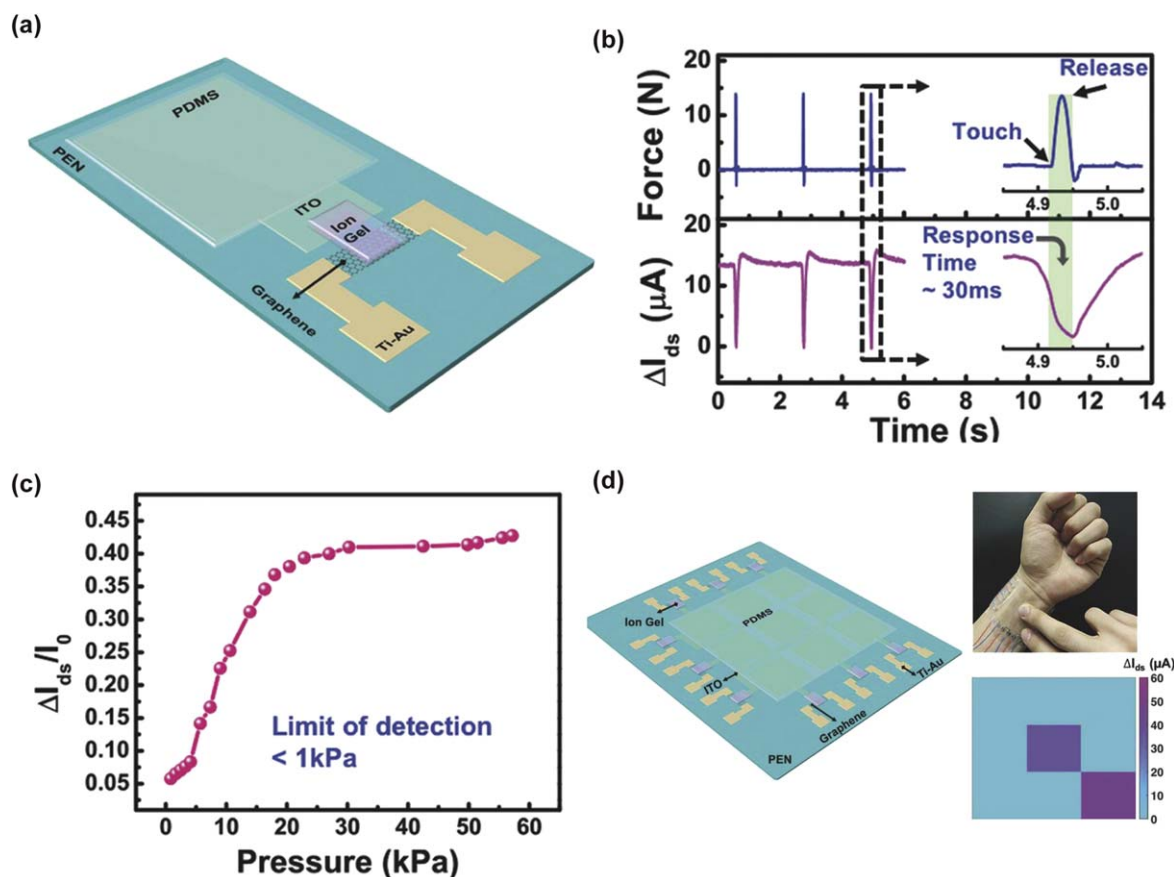


**Figure 10.** Graphene tribotronics for electronic skin. (a) Schematic diagram of the graphene tribotronic device. (b) Touch signals (top) and  $\Delta I_{ds}$  (bottom); the response time is about 30 ms. (c) The relationship between the normalized current modulation and the touch pressure. (d) Schematic description of a  $3 \times 3$  graphene tribotronic transistors array. [49] John Wiley & Sons. © 2016 WILEY-VCH Verlag GmbH & Co. KGaA, Weinheim.

### 6.2. Top-gated graphene tribotronic transistor

The top-gate structure of FET has many advantages, such as simple integration process, low cost and stability towards fully flexible device. The top-gated graphene tribotronic transistor was realized on a Si/SiO<sub>2</sub> substrate [50] (figure 11(a)). Using the spin coating method, the PDMS and PMMA covered on the top surface of the graphene as a fixed frictional layer. In order to induce opposite charges on the

fixed frictional layers, Acrylic and PDMS are specially selected as their corresponding frictional layer, respectively. When the positively charged Acrylic (negatively charged PDMS) frictional layer approach and leave the transistor with minimum distance about 2 mm, the resistance variety of the graphene channel is about 0.14% to 0.5% (figure 11(b)). When the external object has a temporary contact with the fixed frictional layer, the resistance of the graphene channel

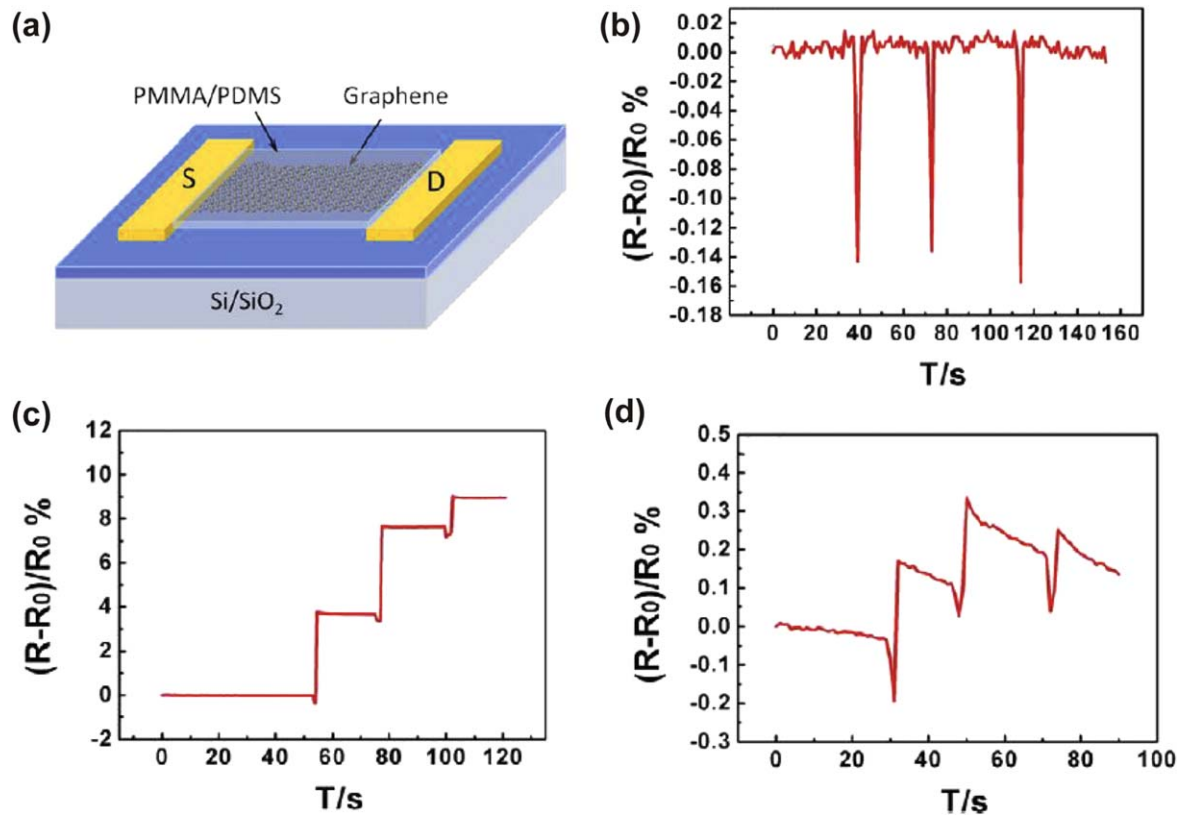


**Figure 11.** Top-gated graphene tribotronic transistor. (a) Schematic of a graphene channel with PMMA or PDMS fixed frictional layer. (b), (c) The relative change of the graphene channel resistance in the approach-and-leave and attach-and-detach models. (d) The experimental results of the control device without passive layer in the attach-and-detach test. Reprinted from [50], Copyright 2017, with permission from Elsevier.

increases (decreases) step by step (figure 11(c)). It should be noted that the device with  $2\ \mu\text{m}$  thickness PMMA fixed frictional layer shows larger resistance change than the device with  $60\ \mu\text{m}$  thickness PDMS fixed frictional layer (figure 11(d)). This work has developed a new structure tribotronic transistor with two operation models and has wide application in tactile sensors and pressure sensors.

### 6.3. Rewritable ghost floating gates by tunneling triboelectrification for 2D electronics

The conventional FET is using external gate bias voltage to tune charge carriers in a semiconductor material. In the very large-scale integration, the integrating independent FETs fabricated on a single chip are very difficult and complex. Moreover, once the circuit has been manufactured, it is difficult to modify the structure and position of the gates. By using tunneling triboelectrification, dynamically localizing charges are generated to form anfloating, immaterial, bottom ghost gate underneath graphene [51]. A Pt-coated AFM tip was used to rub with the CVD graphene ( $0.5 \times 0.5\ \mu\text{m}^2$ ) and then a part of the triboelectric charges tunnel through graphene and are stuck at the interface among the air-gap and the insulation layer (figure 12(a)). The potential difference has good stability, in which it only show a little decay after 72 h (figure 12(b)). It is worth noting that the tunneling triboelectrification increases with the decreases of the graphene

layer number, and not occurs in HOPG or high-quality mechanical exfoliated graphene (figure 12(c)).

Compared with traditional electronic devices, which cannot be changed after fabricating, the most important characteristic of the device is that both the polarity and quantity of the trapped charges of graphene can be tuned by using a biasing voltage to the rubbing Pt AFM tip. As a proof of concept, the rewritable  $p/p^+$  and  $p/n^+$  junctions were drawn, in which the resolution is about 200 nm (figure 12(d)). Furthermore, the resistivity and the Dirac point of graphene can be tuned by the tunneling triboelectrification. This work has proved the function of the tunneling triboelectrification in large-scale integration of independent 2D FET, and open up a new way to fabricate rewritable 2D electronics.

## 7. Tribotronic functional devices

### 7.1. Flexible transparent tribotronic transistor

Because of material diversity and the admirable performance, the tribotronics has tremendous application prospects in intelligent human-machine interaction and active flexible electronics. By the conjunction of a TENG in free-standing sliding mode and an organic thin film transistor (OTFT), a novel flexible transparent tribotronic transistor (FTT) has been developed, which is using flexible and transparent

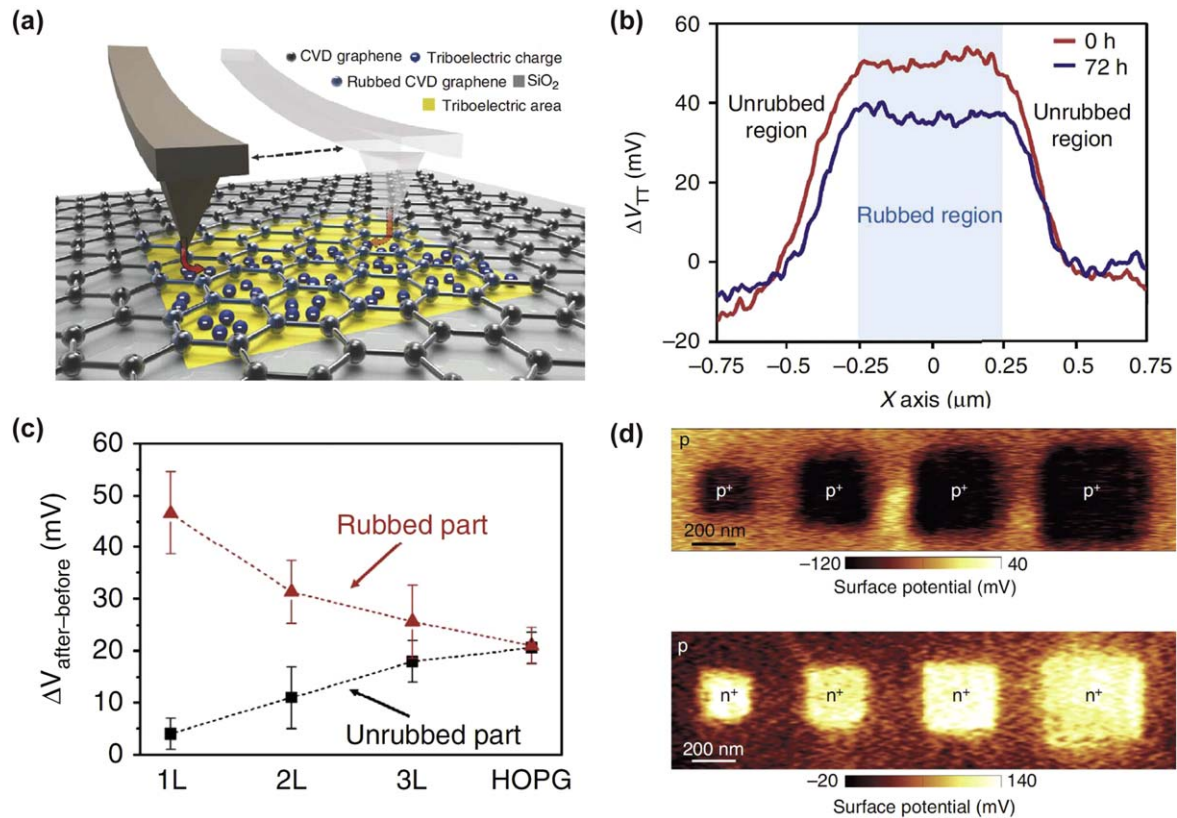


**Figure 12.** Rewritable ghost floating gates by tunneling triboelectrification for 2D electronics. (a) Schematic diagram of the rubbing process using KPFM. (b) Potential difference produced by tunneling triboelectrification (0 and 72 h). (c)  $\Delta V_u$  and  $\Delta V_r$  for HOPG and different thickness CVD graphene. (d) Rewritable  $p/n^+$  and  $p/p^+$  junctions and ghost floating gates. Reproduced from [51]. CC BY 4.0.

materials [20] (figure 13(a)). The FTT has a traditional back-gate OTFT structure of ITO/Ta<sub>2</sub>O<sub>5</sub>/pentacene fabricated on a flexible PET film, and the TENG has a structure of two ITO electrodes which are electric connected to the source and gate electrodes, respectively. The bottom of the PET substrate is etched with a size of 10 mm × 10 mm along y-axis. A FEP film was pasted on the surface of the bottom PET as the free-standing sliding layer. As shown in figure 13(b), in the visible wavelength range, the optical transparency of the FTT device can reach to 71.6%. And the logo on the paper can be clearly seen through the device, showing a good transmittance of the device.

The  $I_{ds}-V_{ds}$  characteristics of the FTT at different sliding distance are demonstrated. The drain current increases from 2 to 22 μA when the sliding distance increases in a range of 0–7 mm (figure 13(c)). Furthermore, the performance of the FTT can be retained under several bending radius and modes, exhibiting a great mechanical flexibility (figure 13(d)). The FTT could be used as an active modulation mechanism in electronic skin to modulate conventional electronics, including the sound intensity, magnetic intensity, micro-motion and luminance (figures 13(e) and (f)). This work has presented a flexible and transparent tribotronic transistor and a new way to continuously and actively tune conventional electronics.

## 7.2. Tribotronic transistor array as an active tactile sensing system

Based on the CE-FET, a flexible 10 × 10 tribotronic transistor array (TTA) is produced for active tactile sensing by the conjunction of triboelectric nanogenerators and FET units [18] (figure 14(a)). A single transistor unit (0.5 × 0.5 mm<sup>2</sup>) in the array, composed by a commercial diode and an n-type transistor, and the source electrode of the n-type transistor is electric connected with the anode of the diode (figure 14(b)). This structure makes sure that the drain–source current ( $I_{DS}$ ) pass through the transistor unidirectionally. By the corresponding external contact, the  $I_{DS}$  of each tribotronic transistor can be individually tuned, thereby inducing a local bias voltage to use as the conventional ‘gate’ voltage ( $V_{GS}$ ). As the distance between a certain copper (Cu) pad and the mobile electrification layer separated, the resulting  $I_{DS}$  exhibited a changing trend of three typical regions: an initial fast growth within 3 mm, and then a slow increase between 3 and 9 mm, and finally a saturation state over 9 mm (figure 14(c)). Furthermore, the TTA show a high resolution and keep good sensitivity even the size of the pixel is reduced to 0.5 × 0.5 mm<sup>2</sup>. Given this  $I_{DS}$  change against external stimuli, the TTA then is applied to realize multipoint sensing, real-time trajectory tracing and dynamic motion monitoring.

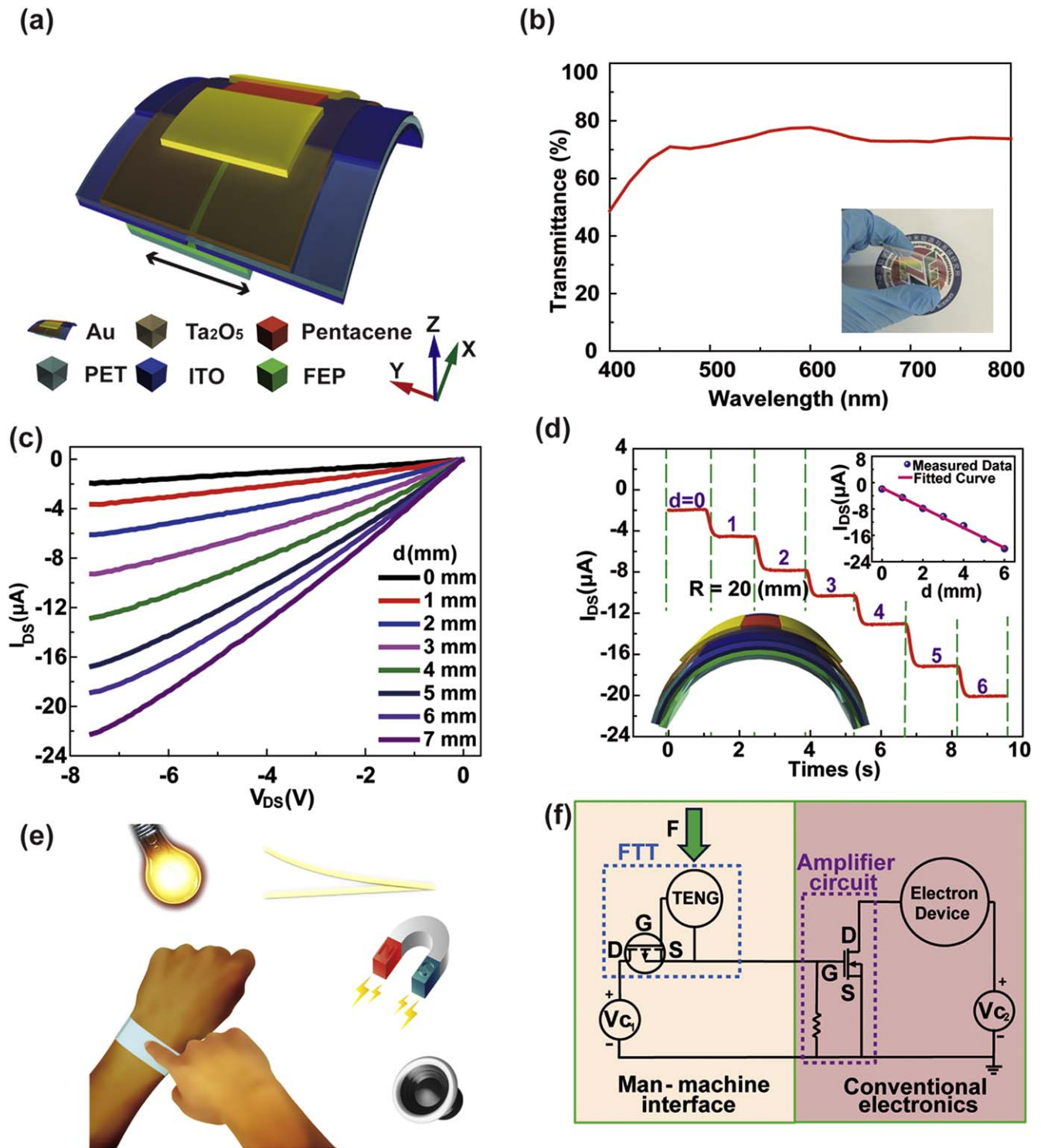


**Figure 13.** Flexible transparent tribotronic transistor. (a) Structure of the FTT. (b) Transmittance characteristics of the FTT. (c)  $I_{DS}$ - $V_{DS}$  curves of the FTT with different sliding distances. (d)  $I_{DS}$  output characteristics ( $V_{DS} = -8$  V) with different sliding distances under tensile strain status. (e), (f) Schematic diagram and equivalent circuit of the wearable FTT for active modulation of several conventional electronics. Reprinted from [20], Copyright 2017, with permission from Elsevier.

In addition, the sensing capability of the active tactile sensing system has been displayed by putting letter-shaped external object onto the surface of a flexible  $10 \times 10$  TTA. The reconstruction of the 'letter' image in figure 14(d) clearly indicates that the contour of objects can be accurately

identified and further mapped via 2D current intensity map. The TTA has realized the coupling of triboelectrification and traditional integrated circuits, and it has potential application in the field of flexible/wearable electronics and active tactile sensing systems.

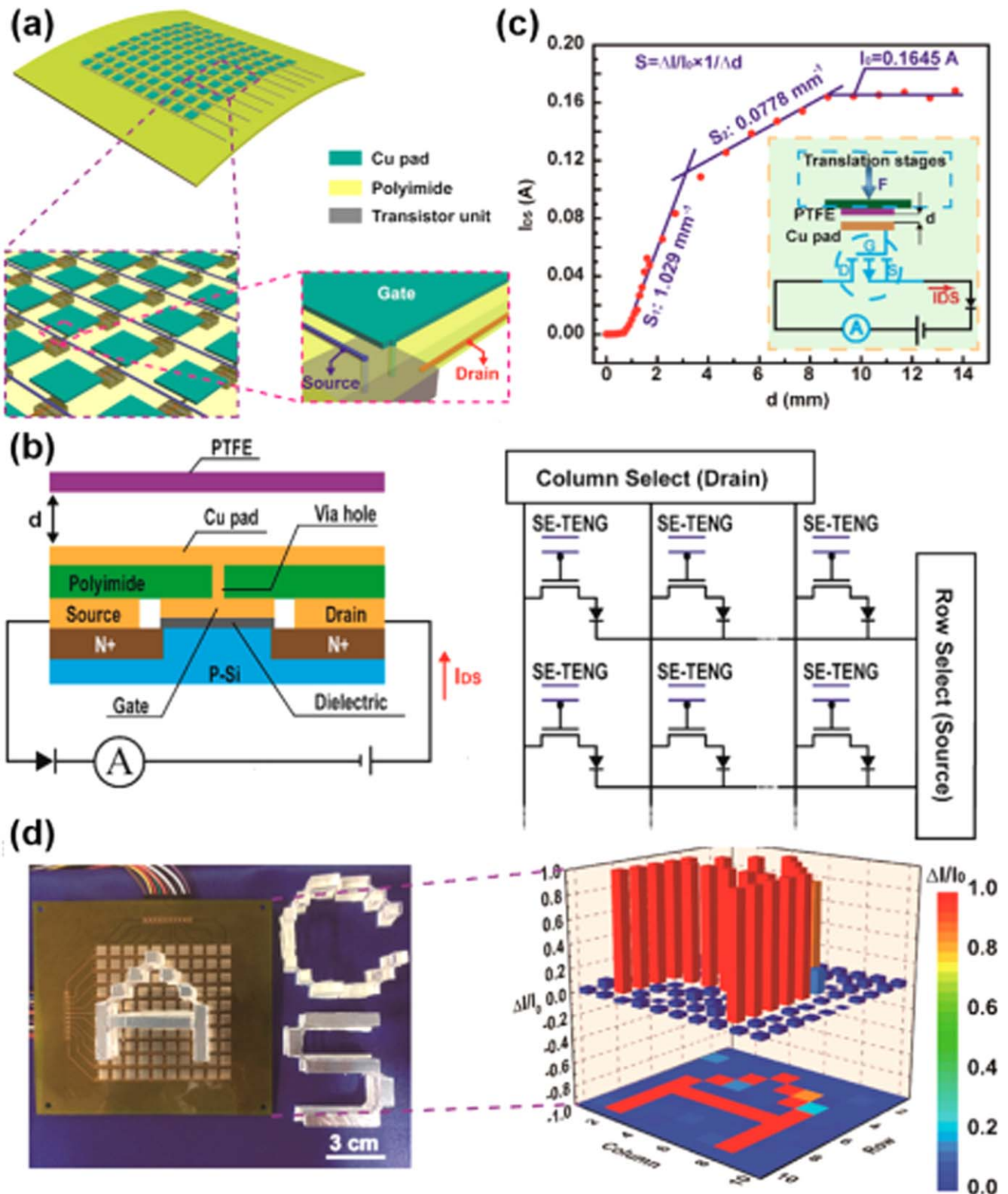


**Figure 14.** Tribotronic transistor array as an active tactile sensing system. (a) Schematic of a 10 × 10 TTA. (b) Sketch of a single pixel and equivalent circuit schematic of the active tactile sensing system. (c) The relationship between the output current of a single pixel and the separation distance. (d) Photograph of a 10 × 10 TTA and the corresponding 3D and 2D normalized  $I_{DS}$  intensity map of the A-shaped letter. Reprinted with permission from [18]. © 2016, American Chemical Society

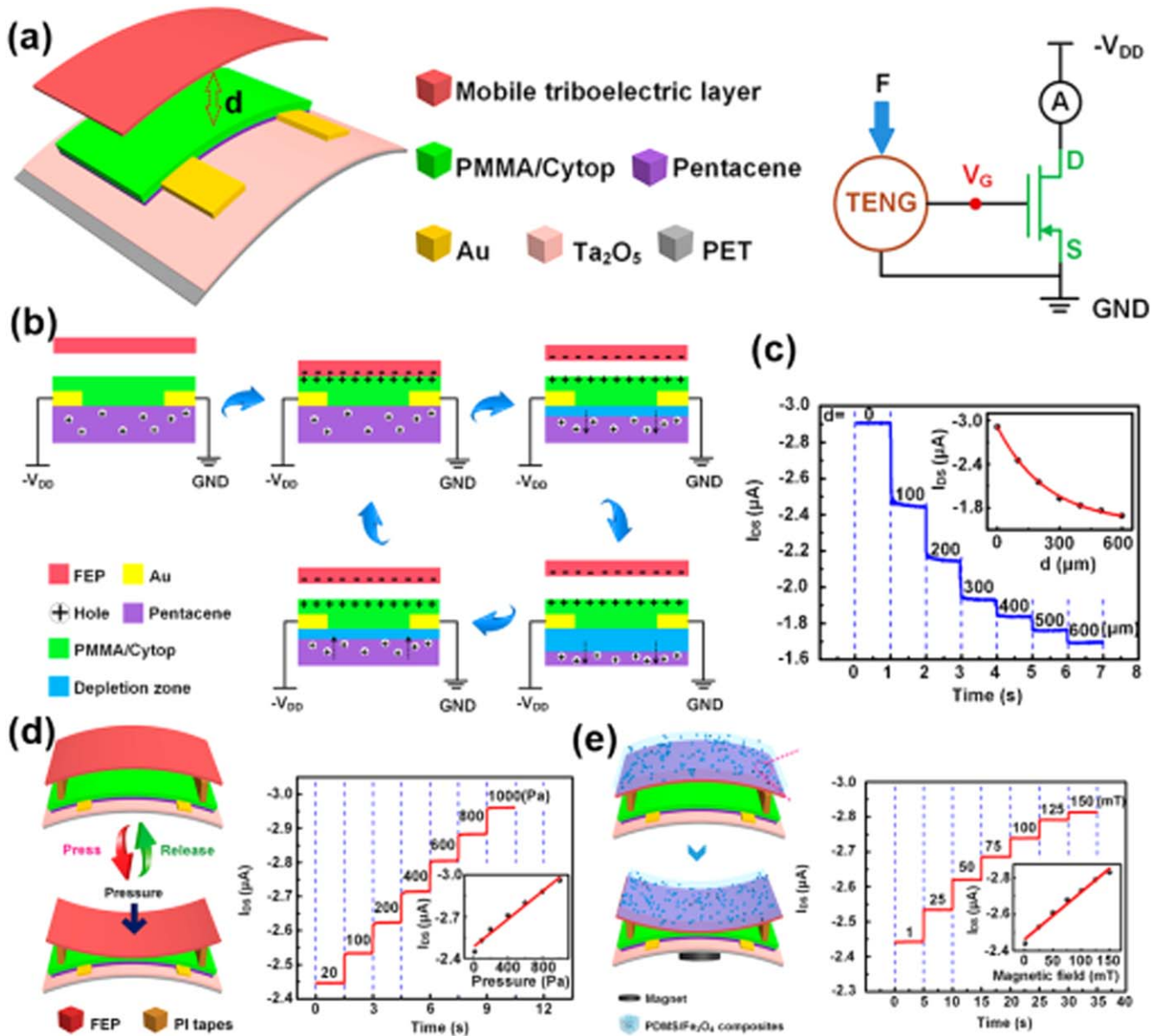


**Figure 15.** Flexible organic tribotronic transistor (FOTT) for pressure and magnetic sensing. (a) Structure of the FOTT without a top gate electrode. The inset is equivalent circuit diagram of the device. (b) Schematic working principle of the FOTT. (c)  $I_{DS}$  output characteristics with different separation distances. (d) Schematic illustration of the pressure sensor and its  $I_{DS}$  output characteristics. (e) Schematic illustration of the FOTT for magnetic sensing structure and its  $I_{DS}$  output characteristics. Reprinted with permission from [22]. © 2017, American Chemical Society

### 7.3. Flexible organic tribotronic transistor (FOTT)

To address the issue of the complexity of manufacturing independent gates for tribotronic transistor, a FOTT has been developed [22], in which the top gate electrode is removed. The FOTT, uses a flexible PET film, poly (methyl methacrylate)/Cytop (PMMA/Cytop) composites and the *p*-type pentacene as substrate layer, dielectric layer and semiconductor layer, respectively (figure 15(a)). By using the external press, the TENG can generate an electrical potential difference to modulate the  $I_{DS}$  of the transistor without a top gate electrode (figures 15(b) and (c)). Based on the FOTT (figure 15(d)), the authors have developed a pressure sensor, with a fluorinated ethylene propylene (FEP) film working as

the mobile frictional layer. The  $I_{DS}$  increases as the FEP film gradually comes into contact with the PMMA/Cytop layer. This unique feature can also be utilized to resolve slight change of pressure. In addition to the pressure sensing characteristic, the FOTT is also highlighted by being a noncontact magnetic sensor (figure 15(e)). By mingling magnetic composites with the triboelectric layer, the FOTT-based magnetic sensor has revealed its attractive performance of magnetic sensing.

As a novel gate-free organic tribotronic transistor, the FOTT exhibits low response time, high pressure sensitivity and excellent stability. In the meantime, this work finds new applications in magnetic sensing, which shows huge potentials of tribotronics in active smart electronic skins, intelligent



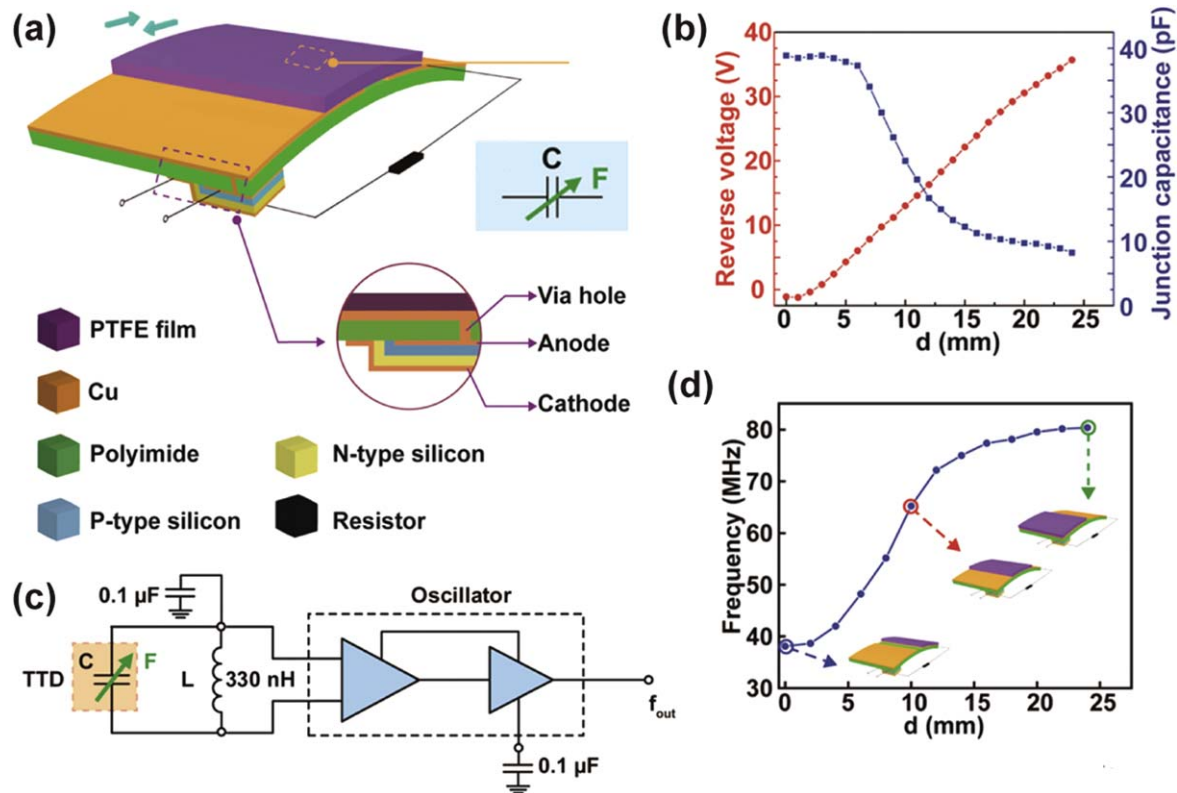


**Figure 16.** Tribotronic tuning diode for active analog signal modulation. (a) Schematic illustration of the TTD. (b) Output reverse voltage from the TENG and the junction capacitance as a function of the sliding distance of the PTFE film. (c) Schematic circuit diagram of the frequency modulation by TTD in conjunction. (d) Frequency distribution of the modulated sinusoidal signals. Reprinted with permission from [52]. © 2017, American Chemical Society

sensing, flexible and wearable electronics, human–machine interaction, etc.

#### 7.4. Tribotronic tuning diode (TTD) for active analog signal modulation

The aforementioned works are all based on the model of a tribotronic transistor, in which the carrier transport can be tuned by the electrostatic potential that applies on a metal–insulator–semiconductor capacitor. As another type of capacitive load, the  $p$ – $n$  junction capacitor in a diode is able to be effectively modulated by the electrostatic potential. Accordingly, a TTD is developed by coupling a variable capacitance diode and a TENG in free-standing mode [52]. It mainly consists of a flexible polyimide substrate, two Cu pads, a free-standing polytetrafluoroethylene (PTFE) film as a friction layer, a variable capacitance diode, and a resistor (figure 16(a)). When the friction layer slides on the device surface for triboelectrification, a reverse bias voltage is produced and applied to the  $p$ – $n$  junction for modulating the junction capacitance. As the sliding distance increases from 0 to 25 mm, the capacitance of the TTD changing from about 39 to 8 pF (figure 16(b)), which is considerably appropriate to actively modulate analog signal. As illustrated in the circuit diagram of the frequency modulation by TTD (figure 16(c)), the frequency of the output signal ( $f_{\text{out}}$ ) was solely determined by the capacitance of the TTD, which is closely related to the sliding distance of the friction layer. When the friction layer

remained at the initial position (on the right Cu pad), the frequency of the  $f_{\text{out}}$  displayed a minimum value. An apparent frequency increase to about 81.5 MHz appeared when the sliding distance increased from 0 to 25 mm (figure 16(d)). The result verified that the TTD was an effective tool for modulating the frequency.

The TTD has also demonstrated exceptional performances in phase shift, and low-pass filtering by just sliding a finger. Discriminating from previous tribotronic devices, the TTD has exhibited a tunable diode for active analog signal modulation by tribotronics and expanded the application of the TENG as a tribo-controlled source for capacitive devices. This work might be a promising substitute for common variable capacitance diodes or tunable capacitors in a variety of potential applications such as precise tuning circuits, signal processing, smart wearable devices, active sensor networks, and so on.

#### 7.5. Bioinspired tribotronic resistive switching memory

Apart from the transistor-based and diode-based electronics, expanded applications of tribotronics have successfully been realized in resistive switching memory. In this touching sensing-memorizing-integrated system, the resistive random access memory (RRAM) is fabricated with a Au/Ta<sub>2</sub>O<sub>5</sub>/AZO structure, and the TENG is composed of a PTFE film and Al electrodes array [53] (figure 17(a)). The device exhibits an exceptional touching response and the responsivity reaches

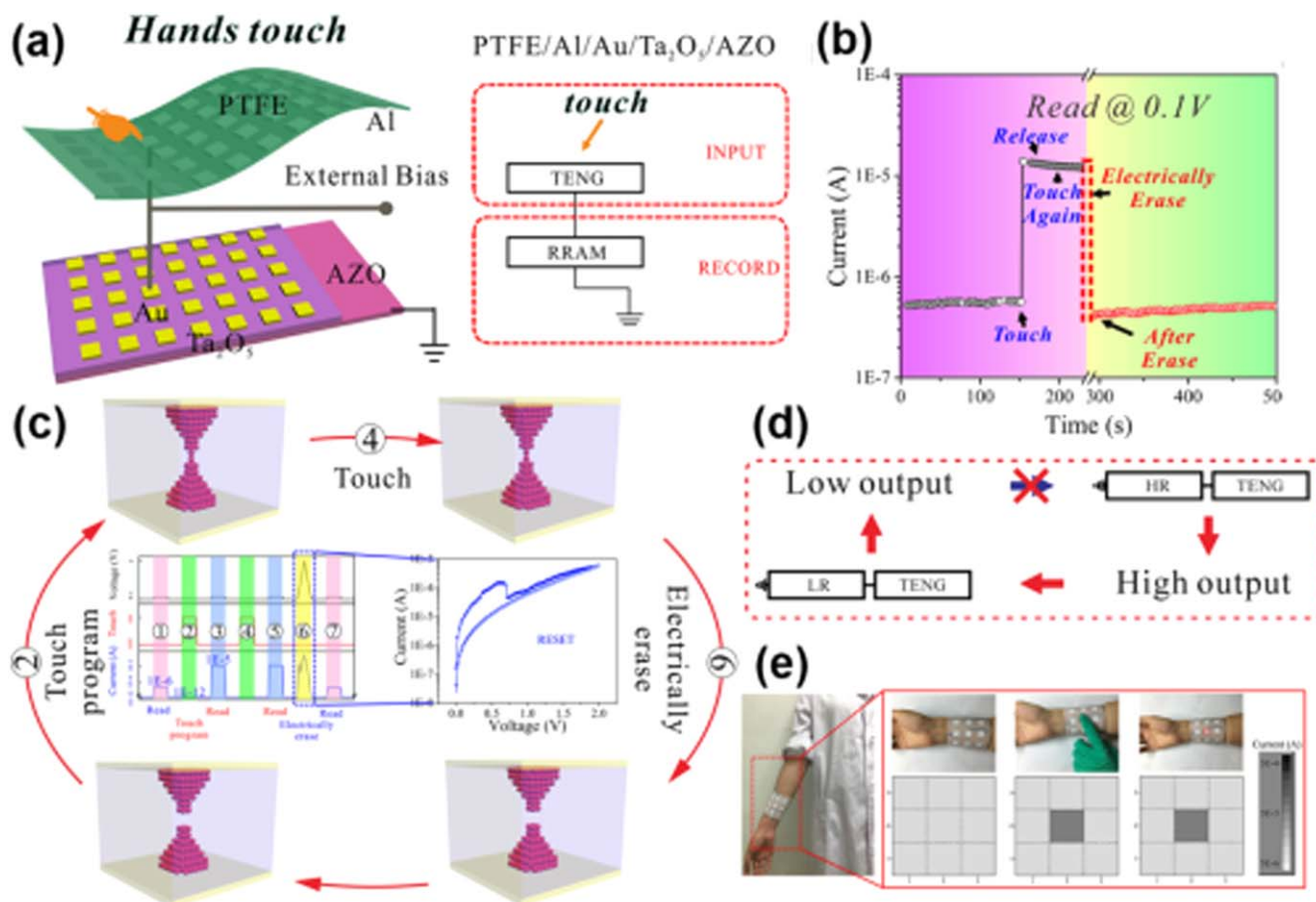


**Figure 17.** Bioinspired tribotronic resistive switching memory for self-powered memorizing mechanical stimuli. (a) Schematic diagram of the integrated system. (b) Current response with touching action at the reading voltage of 0.1 V, and the performance after electrically erasing. (c) Series of measurements, including responsive test, nonvolatile test, anti-interference test and recoverable test. (d) Simplified mechanism diagram of integrated system in a whole cycle. (e) Photograph of cell matrix with  $3 \times 3$  pixels and corresponding current mapping before, in and after press. Reprinted with permission from [53]. © 2017, American Chemical Society.

20 times even with a bias of 0.1 V (figure 17(b)). Through a set of measurements without external bias, including responsive test, nonvolatile test, anti-interference test and recoverable test (figure 17(c)), the system has successfully been employed to realize touching-programming and electrical erasing, featuring the function of tactile memory and reusability. As for the working mechanism, it can be simply described as that high potential difference shifts RRAM device from high resistive state (HRS) to low resistive state (LRS), while the small potential difference is useless for resistive switching of RRAM (figure 17(d)). On this basis, the skin touching only switches the memory device once: from HRS to LRS, hence effectively avoiding the drawback of bipolar output voltage of the TENG. In this system, RRAM and TENG devices are integrated to achieve the functions of fully self-powered, nonvolatile sensing and memorizing (figure 17(e)). When touch action is applied on the middle cell of the  $3 \times 3$  array, the corresponding current signal becomes higher, whereas others remain unchanged. Even if the finger is removed or touches again, this current change keeps invariable. In addition, the implemented integrated system array demonstrates the ability of memorizing the finger motion trajectory in 2D space. The rise of fully self-

powered, sensing-memorizing-integrated system may open up new avenues for the next generation high-performance smart systems for applications in electronic skins, smart sensors, and artificial intelligence.

## 8. Theoretical simulation of tribotronics

### 8.1. Theoretical study of tribotronic MOSFET performances

A FEM has been utilized to simulate characteristics of tribotronic MOSFET by the COMSOL software [54]. The basic structure of CE tribotronic transistor (CG NMOS) built in the FEM is consisted of a silicone based NMOS and a mobile layer that is a PTFE film (25 nm thick) with Al deposited on the back side (figure 18(a)). In addition, the conduction channel length  $L$  is set as  $1 \mu\text{m}$  and the separation distance  $d$  between gate electrode and PTFE film changes from 1 nm to  $3 \mu\text{m}$ . Other parameters including doping profile, doping concentration, and the detailed geometrical dimension are set as appropriate values. Moreover, when the electrode on the mobile layer is electric connected to the grounded source and bulk electrodes, the working mode of CG NMOS is defined as

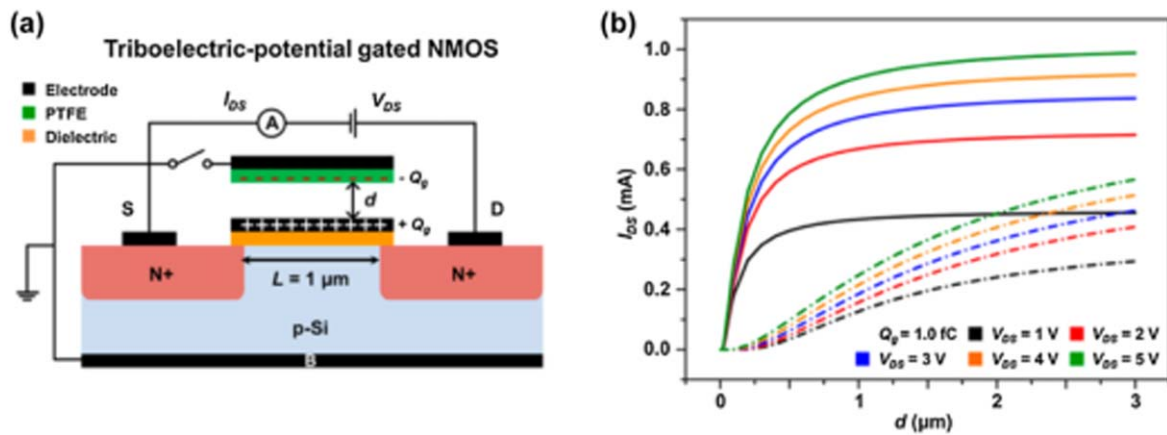


**Figure 18.** Theoretical analysis on the performances of the contact electrification tribotronic MOSFET. (a) Schematic illustration of the contact electrification tribotronic NMOS. (b)  $I_{DS}$ - $d$  characteristics of the contact electrification tribotronic NMOS with different  $V_{DS}$  from 1 to 5 V. Reprinted with permission from [54]. © 2016, American Chemical Society

‘w/feedback’. On the contrary, ‘w/o feedback’ is that the mobile layer acts as the floating layer, which is isolated from all the electrodes. According to the triboelectric series that Al is easier to lose electrons than PTFE, there could be an equal amount of opposite charges on their contact surface. As shown in figure 18(b),  $I_{DS}$  enhances gradually with the increasing of  $d$ , which is similar to the traditional NMOS in ‘w/o feedback’ mode. While in the ‘w/feedback’ mode,  $I_{DS}$  quickly enhances at first and then approaches a saturation at last, which demonstrates that it could be used as a tune switch with a fast response speed by moving the mobile layer away from gate electrode for a very short distance about hundreds of nanometers.

### 8.2. Theoretical study of sliding-electrification-gated tribotronic transistors and logic device

As for the sliding electrification gated tribotronic transistor (SG NMOS) built in the FEM, a PTFE film with a thickness of 25 nm is set on the gate electrode of NMOS (figure 19(a)) [55]. When the PTFE film gradually slides by the external force, an electrostatic potential is produced on the gate electrode, which could serve as the gate voltage to control the transportation of carriers between drain and source. As shown in figure 19(b), with the increases of the sliding distance  $x$  from 0 to 1.5  $\mu\text{m}$ , the  $I_{DS}$  maintains almost zero firstly, and then it enhances gradually with an increasing slope, which is similar to the traditional silicon-based NMOS in enhancement mode. When the PTFE layer is adhered on the gate electrode, and a nylon film is selected to rub with the PTFE layer (figure 19(c)), a depletion mode SG NMOS is also built. Meanwhile, with the sliding distance  $x$  increasing, the VGS decreases gradually to negative values, which could further reduce the  $I_{DS}$  (figure 19(d)).

Based on two SG NMOSs, a sliding electrification gated tribotronic logic device (SGL) is further built in the FEM, in which a PTFE film is set on the two gate electrodes and the distance between two SG NMOSs was set as 1  $\mu\text{m}$ . As shown in figure 19(e), the source electrode of left SG NMOS and the drain electrode of right SG NMOS are connected to ground

and a power source of  $V_{\text{bias}}$ , respectively. At the same time, as the  $V_{\text{out}}$  of SGL, the source electrode of right SG NMOS is connected to the drain electrode of left SG NMOS. When the PTFE layer is slide right gradually, different electrostatic potentials are generated on the two gate electrodes, which could result in a logic level signal output. The  $V_{\text{out}}$  of SGL is reduced with the increasing of sliding distance  $x$  (figure 19(f)), in which the  $V_{\text{out}}$  above 0.9 V is set as logic ‘1’, while the  $V_{\text{out}}$  below 0.1 V is set as logic ‘0’ for the SGL. As a result, logic ‘1’ could be transformed into logic ‘0’, with the sliding distance  $x$  enhancing from 0 to 1.5  $\mu\text{m}$ . These results demonstrate that the  $V_{\text{out}}$  of SGL could be tuned by the external mechanical force, which has potential applications in MEMS, sensing terminal and human-machine interaction.

## 9. Summary and perspectives

Since piezotronics were introduced by Zhong Lin wang in 2006, this field has seen rapid development and wide applications. Some important II-VI and III-V wurtzite semiconductors, such as GaN, InN, CdS, and CdSe, are proved to be the excellent piezotronic materials. With the development of nanotechnology, high-quality III-V/II-VI heterojunctions can also be fabricated to effectively modulate the carrier transportation. In addition, the piezotronic modulated carrier transportation is also observed in new material systems, for example Te nanobelt and ZnSnO<sub>3</sub> nanowire, which further deepen our understanding on the piezotronic effect. Thanks to the excellent mechanical and electrical properties, 2D materials, for example MoS<sub>2</sub>, are another important development direction. With these piezoelectric semiconductors, people design and fabricate many novel and high-performance piezotronic devices, such as SGT, tactile imaging, logic devices, chemical/biomedical sensor, and electronic/electrical devices. These diverse and multifunctional devices show another development direction of information technology different from Moore’s law.

Following the proposed piezotronics, tribotronics was first developed in 2014, which is coupled with triboelectricity

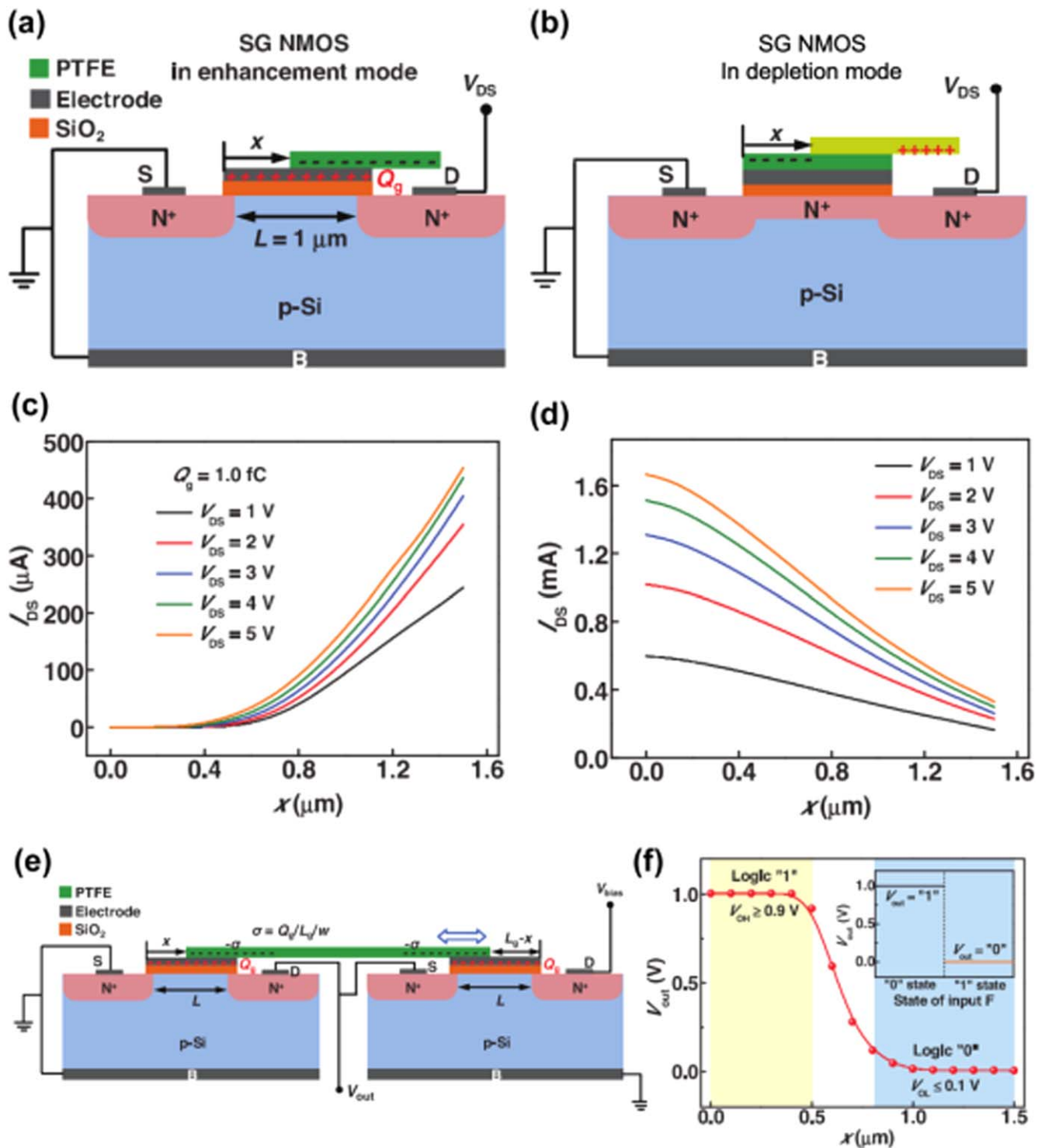


**Figure 19.** Theoretical analysis on the performances of the sliding electrification tribotronic MOSFET (SG NMOS). (a) Schematic diagram of SG NMOS in enhancement mode. (b)  $I_{DS}$ - $x$  relationship of SG NMOS with various  $V_{DS}$ . (c) Schematic diagram of SG NMOS in depletion mode. (d)  $I_{DS}$ - $x$  relationship of SG NMOS with various  $V_{DS}$  in depletion mode. (e) Structure of the SGL. (f)  $V_{out}$ - $x$  transfer characteristic of the SGL under a bias voltage of 1 V. The logic '1' output region at  $V_{OH} \geq 0.9$  V and logic '0' output region at  $V_{OL} \leq 0.1$  V are marked. The insert graph shows the output logic levels at '1' and '0' states. [55] John Wiley & Sons. © 2017 WILEY-VCH Verlag GmbH & Co. KGaA, Weinheim.

and semiconductor. As the fundamental component of tribotronics, the CE FET by coupling traditional FET and TENG is reviewed. The tribotronics have an advantage of selected material diversification, especially the novel 2D materials.




Based on the fundamental tribotronic transistor, several tribotronic functional devices were developed, such as tribotronic tactile sensing system, magnetic sensor, TTD and tribotronic resistive switching memory. Tribotronics has

expanded the emerging fields of nano-electronics and nano-energy, and has important applications in human-machine interface, MEMS/NEMS, sensor and active flexible/wearable electronics.

## Acknowledgments

National Key Research and Development Program of China (2016YFA0202704, 2016YFA0202703), National Natural Science Foundation of China (Grant Nos. 51432005, 61574018, 51475099).

## ORCID iDs

Weiguo Hu  <https://orcid.org/0000-0002-8614-0359>  
 Chi Zhang  <https://orcid.org/0000-0002-7511-805X>  
 Zhong Lin Wang  <https://orcid.org/0000-0002-5530-0380>

## References

- [1] Wang Z L 2012 Progress in piezotronics and piezophotonics *Adv. Mater.* **24** 4632–46
- [2] Wang X D, Zhou J, Song J H, Liu J, Xu N S and Wang Z L 2006 Piezoelectric field effect transistor and nanoforce sensor based on a single ZnO nanowire *Nano Lett.* **6** 2768–72
- [3] Wang Z L and Song J 2006 Piezoelectric nanogenerators based on zinc oxide nanowire arrays *Science* **312** 242–6
- [4] He J H, Hsin C L, Liu J, Chen L J and Wang Z L 2007 Piezoelectric gated diode of a single ZnO nanowire *Adv. Mater.* **19** 781–4
- [5] Wang Z L 2007 Nanopiezotronics *Adv. Mater.* **19** 889–92
- [6] Yu R M, Wu W Z, Ding Y and Wang Z L 2013 GaN nanobelt-based strain-gated piezotronic logic devices and computation *ACS Nano* **7** 6403–9
- [7] Zhou Y *et al* 2013 Nano-newton transverse force sensor using a vertical GaN nanowire based on the piezotronic effect *Adv. Mater.* **25** 883–8
- [8] Ku N J, Huang J H, Wang C H, Fang H C and Liu C P 2012 Crystal face-dependent nanopiezotronics of an obliquely aligned InN nanorod array *Nano Lett.* **12** 562–8
- [9] Lin Y F, Song J, Ding Y, Liu S Y and Wang Z L 2008 Piezoelectric nanogenerator using CdS nanowires *Appl. Phys. Lett.* **92** 022105
- [10] Zhou Y S, Han W, Rai S C, Zhang Y, Ding Y, Pan C, Zhang F, Zhou W and Wang Z L 2012 Vertically aligned CdSe nanowire arrays for energy harvesting and piezotronic devices *ACS Nano* **6** 6478–82
- [11] Kou J, Zhang Y, Liu Y, Zhang K, Liu W and Zhai J 2017 Nano-force sensor based on a single tellurium microwire *Semicond. Sci. Technol.* **32** 074001
- [12] Gao S, Wang Y, Wang R and Wu W 2017 Piezotronic effect in 1D van der Waals solid of elemental tellurium nanobelt for smart adaptive electronics *Semicond. Sci. Technol.* **32** 104004
- [13] Wu J M, Chen C Y, Zhang Y, Chen K H, Yang Y, Hu Y, He J H and Wang Z L 2012 Ultrahigh sensitive piezotronic strain sensors based on a ZnSnO<sub>3</sub> nanowire/microwire *ACS Nano* **6** 4369–74
- [14] Fan F R, Tian Z Q and Wang Z L 2012 Flexible triboelectric generator *Nano Energy* **1** 328–34
- [15] Zhang C, Tang W, Han C B, Fan F R and Wang Z L 2014 Theoretical comparison, equivalent transformation, and conjunction operations of electromagnetic induction generator and triboelectric nanogenerator for harvesting mechanical energy *Adv. Mater.* **26** 3580–91
- [16] Zhang C, Tang W, Zhang L M, Han C B and Wang Z L 2014 Contact electrification field-effect transistor *ACS Nano* **8** 8702–9
- [17] Zhang C and Wang Z L 2016 Tribotronics—a new field by coupling triboelectricity and semiconductor *Nano Today* **11** 521–36
- [18] Yang Z W, Pang Y, Zhang L, Lu C, Chen J, Zhou T, Zhang C and Wang Z L 2016 Tribotronic transistor array as an active tactile sensing system *ACS Nano* **10** 10912–20
- [19] Wu J M, Lin Y H and Yang B Z 2016 Force-pad made from contact-electrification poly (ethylene oxide)/InSb field-effect transistor *Nano Energy* **22** 468–74
- [20] Pang Y, Li J, Zhou T, Yang Z, Luo J, Zhang L, Dong G, Zhang C and Wang Z L 2017 Flexible transparent tribotronic transistor for active modulation of conventional electronics *Nano Energy* **31** 533–40
- [21] Li J, Zhang C, Duan L, Zhang L M, Wang L D, Dong G F and Wang Z L 2016 Flexible organic tribotronic transistor memory for a visible and wearable touch monitoring system *Adv. Mater.* **28** 106–10
- [22] Zhao J, Guo H, Pang Y, Xi F, Yang Z, Liu G, Guo T, Dong G, Zhang C and Wang Z L 2017 Flexible organic tribotronic transistor for pressure and magnetic sensing *ACS Nano* **11** 11556–73
- [23] Xue F, Chen L B, Wang L F, Pang Y K, Chen J, Zhang C and Wang Z L 2016 MoS<sub>2</sub> tribotronic transistor for smart tactile switch *Adv. Funct. Mater.* **26** 2104–9
- [24] Pang Y K, Xue F, Wang L F, Chen J, Luo J J, Jiang T, Zhang C and Wang Z L 2016 Tribotronic enhanced photoresponsivity of a MoS<sub>2</sub> phototransistor *Adv. Sci.* **3** 1500419
- [25] Pang Y K, Chen L B, Hu G F, Luo J J, Yang Z W, Zhang C and Wang Z L 2017 Tribotronic transistor sensor for enhanced hydrogen detection *Nano Res.* **10** 3857–64
- [26] Zhang C, Zhang Z H, Yang X, Zhou T, Han C B and Wang Z L 2016 Tribotronic phototransistor for enhanced photodetection and hybrid energy harvesting *Adv. Funct. Mater.* **26** 2554–60
- [27] Zhang Y, Liu Y and Wang Z L 2011 Fundamental theory of piezotronics *Adv. Mater.* **23** 3004–13
- [28] Liu W, Zhang A, Zhang Y and Wang Z L 2015 First principle simulations of piezotronic transistors *Nano Energy* **14** 355–63
- [29] Pal J, Tse G, Haxha V and Migliorato M A 2011 Second-order piezoelectricity in wurtzite III–N semiconductors *Phys. Rev. B* **84** 085211
- [30] Al-Zahrani H Y S, Pal J and Migliorato M A 2013 Non-linear piezoelectricity in wurtzite ZnO semiconductors *Nano Energy* **2** 1214–7
- [31] Al-Zahrani H Y S, Pal J, Migliorato M A, Tse G and Yu D 2015 Piezoelectric field enhancement in III–V core-shell nanowires *Nano Energy* **14** 382–91
- [32] Wang X, Yu R, Jiang C, Hu W, Wu W, Ding Y, Peng W, Li S and Wang Z L 2016 Piezotronic effect modulated heterojunction electron gas in AlGaIn/GaN/GaN heterostructure microwire *Adv. Mater.* **28** 7234–42
- [33] Liu T *et al* 2017 Electrical transportation and piezotronic-effect modulation in AlGaIn/GaN MOS HEMTs and unpassivated HEMTs *Nano Energy* **39** 53–9
- [34] Jiang C *et al* 2017 Piezotronic effect tuned AlGaIn/GaN high electron mobility transistor *Nanotechnology* **28** 455203
- [35] Zhao Z, Pu X, Han C, Du C, Li L, Jiang C, Hu W and Wang Z L 2015 Piezotronic effect in polarity-controlled GaN nanowires *ACS Nano* **9** 8578–83

- [36] Wang C H, Liao W S, Ku N J, Li Y C, Chen Y C, Tu L W and Liu C P 2014 Effects of free carriers on piezoelectric nanogenerators and piezotronic devices made of GaN nanowire arrays *Small* **10** 4718–25
- [37] Yu R, Wang X, Peng W, Wu W, Ding Y, Li S and Wang Z L 2015 Piezotronic effect in strain-gated transistor of a-axis GaN nanobelt *ACS Nano* **9** 9822–9
- [38] Wang X, Yu R, Peng W, Wu W, Li S and Wang Z L 2015 Temperature dependence of the piezotronic and piezophototronic effects in a-axis GaN nanobelts *Adv. Mater.* **27** 8067–74
- [39] Wu W *et al* 2014 Piezoelectricity of single-atomic-layer MoS<sub>2</sub> for energy conversion and piezotronics *Nature* **514** 470–4
- [40] Wu W, Wen X and Wang Z L 2013 Taxel-addressable matrix of vertical-nanowire piezotronic transistors for active and adaptive tactile imaging *Science* **340** 952–7
- [41] Zhou J, Gu Y, Fei P, Mai W, Gao Y, Yang R, Bao G and Wang Z L 2008 Flexible piezotronic strain sensor *Nano Lett.* **8** 3035–40
- [42] Wu W Z, Wei Y G and Wang Z L 2010 Strain-gated piezotronic logic nanodevices *Adv. Mater.* **22** 4711–5
- [43] Niu S M, Hu Y F, Wen X N, Zhou Y S, Zhang F, Lin L, Wang S H and Wang Z L 2013 Enhanced performance of flexible ZnO nanowire based room-temperature oxygen sensors by piezotronic effect *Adv. Mater.* **25** 3701–6
- [44] Cao X T, Cao X, Guo H, Li T, Jie Y, Wang N and Wang Z L 2016 Piezotronic effect enhanced label-free detection of DNA using a Schottky-contacted ZnO nanowire biosensor *ACS Nano* **10** 8038–44
- [45] Liu S, Wang L, Feng X, Wang Z, Xu Q, Bai S, Qin Y and Wang Z L 2017 Ultrasensitive 2D ZnO piezotronic transistor array for high resolution tactile imaging *Adv. Mater.* **29** 1606346
- [46] Han X, Du W, Chen M, Wang X, Zhang X, Li X, Li J, Peng Z, Pan C and Wang Z L 2017 Visualization recording and storage of pressure distribution through a smart matrix based on the piezotronic effect *Adv. Mater.* **29** 1701253
- [47] Nomura K, Ohta H, Takagi A, Kamiya T, Hirano M and Hosono H 2004 Room-temperature fabrication of transparent flexible thin-film transistors using amorphous oxide semiconductors *Nature* **432** 488–92
- [48] Crone B, Dodabalapur A, Lin Y, Filas R, Bao Z, LaDuca A, Sarpeshkar R, Katz H and Li W 2000 Large-scale complementary integrated circuits based on organic transistors *Nature* **403** 521–3
- [49] Khan U, Kim T, Ryu H, Seung W and Kim S W 2017 Graphene tribotronics for electronic skin and touch screen applications *Adv. Mater.* **29** 1603544
- [50] Qu W, Liu W, Li X and Wang X 2017 A triboelectric top-gated graphene transistor *Diamond Relat. Mater.* **73** 33–8
- [51] Kim S, Kim T, Lee K, Kim T, Cimini F, Kim S, Hinchet R, Kim S and Falconi C 2017 Rewritable ghost floating gates by tunneling triboelectrification for two-dimensional electronics *Nat. Commun.* **8** 15891
- [52] Zhou T, Yang Z W, Pang Y, Xu L, Zhang C and Wang Z L 2017 Tribotronic tuning diode for active analog signal modulation *ACS Nano* **11** 882–8
- [53] Sun Y, Zheng X, Yan X, Liao Q, Liu S, Zhang G, Li Y and Zhang Y 2017 Bioinspired tribotronic resistive switching memory for self-powered memorizing mechanical stimuli *ACS Appl. Mater. Interfaces* **9** 43822–9
- [54] Peng W, Yu R, He Y and Wang Z L 2016 Theoretical study of triboelectric-potential gated/driven metal–oxide–semiconductor field-effect transistor *ACS Nano* **10** 4395–402
- [55] Jiang T, Zhang L, Zhang X, Zhang C, Peng W, Xiao T and Wang Z L 2018 Theoretical study of sliding-electrification-gated tribotronic transistors and logic device *Adv. Electron. Mater.* **4** 1700337